1

Stress/Strain-Dependent Properties of Hydraulic Conductivity for Fractured Rocks

Yifeng Chen and Chuangbing Zhou
State Key Laboratory of Water Resources and Hydropower Engineering Science,
Key Laboratory of Rock Mechanics in Hydraulic Structural Engineering,
Wuhan University,
P. R. China

1. Introduction

In the last two decades there has seen an increasing interest in the coupling analysis between fluid flow and stress/deformation in fractured rocks, mainly due to the modeling requirements for design and performance assessment of underground radioactive waste repositories, natural gas/oil recovery, seepage flow through dam foundations, reservoir induced earthquakes, etc. Characterization of hydraulic conductivity for fractured rock masses, however, is one of the most challenging problems that are faced by geotechnical engineers. This difficulty largely comes from the fact that rock is a heterogeneous geological material that contains various natural fractures of different scales (Jing, 2003). When engineering works are constructed on or in a rock mass, deformation of both the fractures and intact rock will usually occur as a result of the stress changes. Due to the stiffer rock matrix, most deformation occurs in the fractures, in the form of normal and shear displacement. As a result, the existing fractures may close, open, grow and new fractures may be induced, which in turn changes the structure of the rock mass concerned and alters its fluid flow behaviours and properties. Therefore, the fractures often play a dominant role in understanding the flow-stress/deformation coupling behavior of a rock system, and their mechanical and hydraulic properties have to be properly established (Jing, 2003).

Traditionally, fluid flow through rock fractures has been described by the cubic law, which follows the assumption that the fractures consist of two smooth parallel plates. Real rock fractures, however, have rough walls, variable aperture and asperity areas where the two opposing surfaces of the fracture walls are in contact with each other (Olsson & Barton, 2001). To simplify the problem, a single, average value (or together with its stochastic characteristics) is commonly used to describe the mechanical aperture of an individual fracture. A great amount of work (Lomize, 1951; Louis, 1971; Patir & Cheng, 1978; Barton et al., 1985; Zhou & Xiong, 1996) has been done to find an equivalent, smooth wall hydraulic aperture out of the real mechanical aperture such that when Darcy's law or its modified version is applied, the equivalent smooth fracture yields the same water conducting capacity with its original rough fracture. It is worth noting that clear distinction manifests between the geometrically measured mechanical aperture (denoted by b in the context) and the theoretical smooth wall hydraulic aperture (denoted by b^*), and the former is usually larger in magnitude than the latter due to the roughness of and filling materials in rock fractures (Olsson & Barton, 2001).

The ubiquity of fractures significantly complicates the flow behaviour in a discontinuous rock mass. The primary problem here is how to model the flow system and how to determine its corresponding hydraulic properties for flow analysis. Theoretically, the representative elementary volume (*REV*) of a rock mass can serve as a criterion for selecting a reasonable hydromechanical model. This statement relates to the fact that *REV* is a fundamental concept that bridges the micro-macro, discrete-continuous and stochastic-determinate behaviours of the fractured rock mass and reflects the size effect of its hydraulic and mechanical properties. The *REV* size for the hydraulic or mechanical behaviour is a macroscopic measurement for which the fractured medium can be seen as a continuum. It is defined as the size beyond which the rock mass includes a large enough population of fractures and the properties (such as hydraulic conductivity tensor and elastic compliance tensor) basically remain the same (Bear, 1972; Min & Jing, 2003; Zhou & Yu, 1999; Wang & Kulatilake, 2002). Owing to high heterogeneity of fractured rock masses, however, the *REV* can be very large or in some situations may not exist. If the *REV* does not exist, or is larger than the scale of the flow region of interest, it is no longer appropriate to use the equivalent continuum approach. Instead, the discrete fracture flow approach may be applied to investigate and capture the hydraulic behaviour of the fractured rock masses. However, due to the limited available information on fracture geometry and their connectivity, it is not a trivial task to make a detailed flow path model. Thus, in practice, the equivalent continuum model is still the primary choice to approximate the hydraulic behaviour of discontinuous rocks.

The hydraulic conductivity tensor is a fundamental quantity to characterizing the hydromechanical behaviour of a fractured rock. Various techniques have been proposed to quantify the hydraulic conductivity tensor, based on results from field tests, numerical simulations, and back analysis techniques, etc. Earlier investigations focused on using field measurements (e.g. aquifer pumping test or packer test (Hsieh & Neuman, 1985)) to estimate the three-dimensional hydraulic conductivity tensor. This approach, however, is generally time-consuming, expensive and needs well controlled experimental conditions. Numerical and analytical methods are also used to estimate the hydraulic properties of complex rock masses due to its flexibility in handling variations of fracture system geometry and ranges of material properties for sensitivity or uncertainty estimations. In the literature, both the equivalent continuum approach (Snow, 1969; Long et al., 1982; Oda, 1985; Oda, 1986; Liu et al., 1999; Chen et al., 2007; Zhou et al., 2008) and the discrete approach (Wang & Kulatilake, 2002; Min et al., 2004) are widely applied. In this chapter, however, only the equivalent continuum approach is focused for its capability of representing the overall behaviour of fractured rock masses at large scales.

Among many others, Snow (1969) developed a mathematical expression for the permeability tensor of a single fracture of arbitrary orientation and aperture and considered that the permeability tensor for a network of such fractures can be formed by adding the respective components of the permeability tensors for each individual fracture. Oda (1985, 1986) formulated the permeability tensor of rock masses based on the geometrical statistics of related fractures. Liu et al. (1999) proposed an analytical solution that links changes in effective porosity and hydraulic conductivity to the redistribution of stresses and strains in disturbed rock masses. Zhou et al. (2008) suggested an analytical model to determine the permeability tensor for fractured rock masses based on the superposition principle of liquid dissipation energy. Although slight discrepancy exists between the permeability tensor and the hydraulic conductivity tensor (the former is an intrinsic property determined by fracture geometry of the rock mass, while the latter also considers the effects of fluid viscosity and

gravity), when taking into account the flow-stress coupling effect, the above models presented, respectively, by Snow (1969), Oda (1985) and Zhou et al. (2008) were proved to be functionally equivalent for a certain fluid (Zhou et al., 2008). A common limitation with the above models lies in the fact that the hydraulic conductivity tensor of a fractured rock mass is all formulated to be either stress-dependent or elastic strain-dependent. Consequently, material nonlinearity and post-peak dilatancy are not considered in the formulation of the hydraulic conductivity tensor for disturbed rock masses. To address this problem, Chen et al. (2007) extended the above work and proposed a numerical model to establish the hydraulic conductivity for fractured rock masses under complex loading conditions.

Based on the observation that natural fractures in a rock mass are most often clustered in certain critical orientations resulting from their geological modes and history of formation (Jing, 2003), characterizing the rock mass as an equivalent continuum containing one or multiple sets of planar and parallel fractures with various critical orientations, scales and densities turns out to be a desirable approximation. Starting from this point of view, the deformation patterns of the fracture network can be first characterized by establishing an equivalent elastic or elasto-plastic constitutive model for the homogenized medium. On this basis, a stress-dependent hydraulic conductivity tensor may be formulated for the former for describing the hydraulic behaviour of the rock mass at low stress level and with overall elastic response; and a strain-dependent hydraulic conductivity tensor for the latter for demonstrating the influences of material non-linearity and shear dilatancy on the hydraulic properties after post-peak loading. This chapter mainly presents the research results on the stress/strain-dependent hydraulic properties of fractured rock masses under mechanical loading or engineering disturbance achieved by Chen et al. (2006), Zhou et al. (2006), Chen et al. (2007) and Zhou et al. (2008).

The stress-dependent hydraulic conductivity model (Zhou et al., 2008) was proposed for estimation of the hydraulic properties of fractured rock masses at relatively lower stress level based on the superposition principle of flow dissipation energy. It was shown that the model is equivalent to Snow's model (Snow, 1969) and Oda's model (Oda, 1986) not only in form but also in function when considering the effects of mechanical loading process on the evolution of hydraulic properties. This model relies on the geometrical characteristics of rock fractures and the corresponding fracture network, and demonstrates the coupling effect between fluid flow and deformation. In this model, the pre-peak dilation and contraction effect of the fractures under shear loading is also empirically considered. It was applied to estimate the hydraulic properties of the rock mass in the dam site of the Laxiwa Hydropower Project located in the upstream of the Yellow River, China, and the model predictions have a good agreement with the site observations from a large number of single-hole packer tests.

The strain-dependent hydraulic conductivity model (Chen et al., 2007), on the other hand, was established by an equivalent non-associative elastic-perfectly plastic constitutive model with mobilized dilatancy to characterize the nonlinear mechanical behaviour of fractured rock masses under complex loading conditions and to separate the deformation of weaker fractures from the overall deformation response of the homogenized rock masses. The major advantages of the model lie in the facts that the proposed hydraulic conductivity tensor is related to strains rather than stresses, hence enabling hydro-mechanical coupling analysis to include the effect of material nonlinearity and post-peak dilatancy, and the proposed model is easy to be included in a FEM code, particularly suitable for numerical analysis of hydromechanical problems in rock engineering with large scales. Numerical simulations

were performed to investigate the changes in hydraulic conductivities of a cube of fractured rock mass under triaxial compression and shear loading as well as an underground circular excavation in biaxial stress field at the Stripa mine (Kelsall et al., 1984; Pusch, 1989), and the simulation results are justified by in-situ experimental observations and compared with Liu's elastic strain-dependent analytical solution (Liu et al., 1999).

Unless otherwise noted, continuum mechanics convention is adopted in this chapter, i.e., tensile stresses are positive while compressive stresses are negative. The symbol (:) denotes an inner product of two second-order tensors (e.g., $\boldsymbol{a}:\boldsymbol{b}=a_{ij}b_{ij}$) or a double contraction of adjacent indices of tensors of rank two and higher (e.g., $\boldsymbol{c}:\boldsymbol{d}=c_{ijkl}d_{kl}$), and ($\otimes$) denotes a dyadic product of two vectors (e.g., $\boldsymbol{a}\otimes\boldsymbol{b}=a_ib_j$) or two second-order tensors (e.g., $\boldsymbol{c}\otimes\boldsymbol{d}=c_{ij}d_{kl}$).

2. Stress-dependent hydraulic conductivity of rock fractures

In this section, the elastic deformation behaviour of rock fractures at the pre-peak loading region will be first presented, and then a stress-dependent hydraulic conductivity model will be formulated. The deformation model (or indirectly the hydraulic conductivity model) is validated by the laboratory shear-flow coupling test data obtained by Liu et al. (2002). The main purpose of this section is to provide a theory for developing a stress-dependent hydraulic conductivity tensor for fractured rock masses that will be presented later in Section 4.

2.1 Characterization of rock fractures

One of the major factors that govern the flow behaviour through fractured rocks is the void geometry, which can be described by several geometrical parameters, such as aperture, orientation, location, size, frequency distribution, spatial correlation, connectivity, and contact area, etc. (Olsson & Barton, 2001; Zhou et al., 1997; Zhou & Xiong, 1997). Real fractures are neither so solid as intact rocks nor void only. They have complex surfaces and variable apertures, but to make the flow analysis tractable, the geometrical description is usually simplified. It is common to assume that individual fractures lie in a single plane and have a constant hydraulic aperture. When the fractures are subjected to normal and shear loadings, the fracture aperture, the contact area and the matching between the two opposing surfaces will be altered. As a result, the equivalent hydraulic aperture of the fractures varies with their normal and shear stresses/displacements, which demonstrates the apparent coupling mechanism between fluid flow and stress/deformation (Min et al., 2004).

The aperture of rock fractures tends to be closed under applied normal compressive stress. The asperities of the surfaces will be crushed when their localized compressive stresses exceed their compressive strength. As a large number of asperities are crushed under high compressive stress, the contact area between the fracture walls increases remarkably and the crushed rock particles partially or fully fill the nearby void, which decreases the effective flow area, reduces the hydraulic conductivity of the fracture, and even changes the flow paths through fracture plane. Fig. 1 depicts the increase in contact area of fractures under increasing compressive stresses modelled by boundary element method (Zimmerman et al., 1991).

The coupling process between fluid flow and shear deformation is more related to the roughness of fractures and the matching of the constituent walls. Fig. 2 shows the impact of the fracture structure on the shear stress-deformation coupling mechanism. In Fig. 2(a), the opposing walls of the fracture are well matched so that the fracture always dilates and the hydraulic conductivity increases under shear loading as long as the applied normal stress is

not high enough for the asperities to be crushed. For the state shown in Fig. 2(c), shear loading will result in the closure of the fracture and the reduction in hydraulic conductivity. Fig. 2(b) illustrates a middle state between (a) and (c), and its shearing effect depends on the direction of shear stress. When the matching of a fracture changes from (a) to (b) then to (c) under shear loading, shear dilation occurs. On the other hand, shear contraction takes place from the movement of the matching from (c) to (b) then to (a). In a more complex scenario, shear dilation and shear contraction may happen alternately, resulting in the fluctuation of the hydraulic behaviour of the fractures.

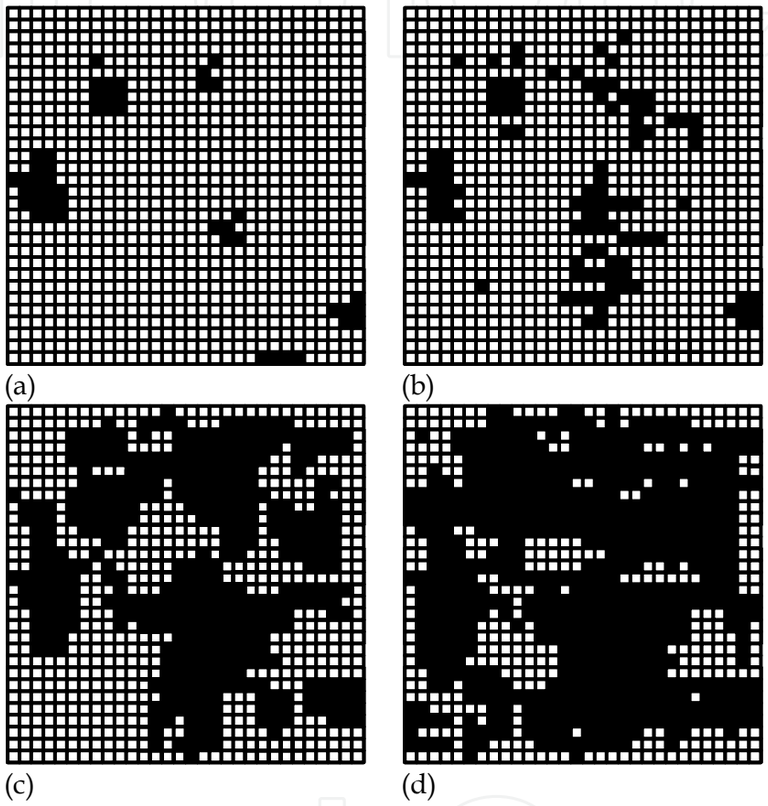

Fig. 1. Variation of contact surface of fractures under increasing compressive stresses (after Zimmerman et al., (1991): (a) P=0 MPa; (b) P=20 MPa; (c) P=40 MPa and (d) P=60 MPa

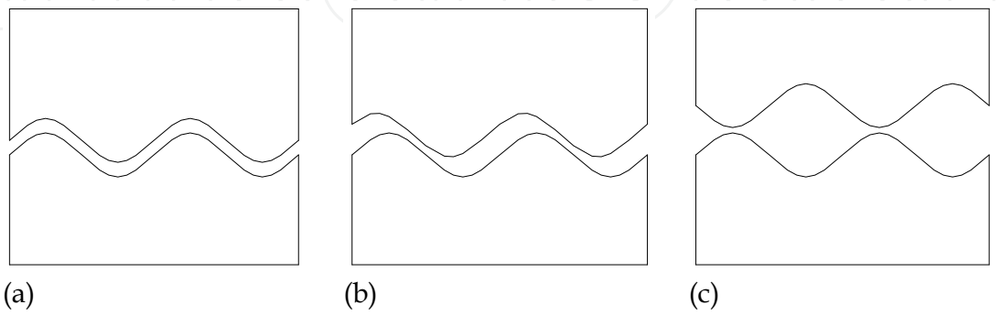

Fig. 2. Shear dilation and shear contraction of fractures: (a) well-matched; (b) fair-matched; and (c) bad-matched

2.2 An elastic constitutive model for rock fractures

To formulate the stress-dependent hydraulic conductivity for rock fractures, we model the fractures by an interfacial layer, as shown in Fig. 3. The interfacial layer is a thin layer with complex constituents and textures (depending on the fillings, asperities and the contact area between its two opposing walls). Assumption is made here that the apparent mechanical response of the interfacial layer can be described by Lame's constant λ and shear modulus μ. Because the thickness of the interfacial layer (i.e., the initial mechanical aperture of the fracture) is generally rather small comparing to the size of rock matrix, it is reasonable to assume that $\varepsilon_x=\varepsilon_y=0$ and $\gamma_{xy}=\gamma_{yx}=0$ within the interfacial layer. Then according to the Hooke's law of elasticity, the elastic constitutive relation for the interfacial layer under normal stress σ_n and shear stress τ can be written in the following incremental form:

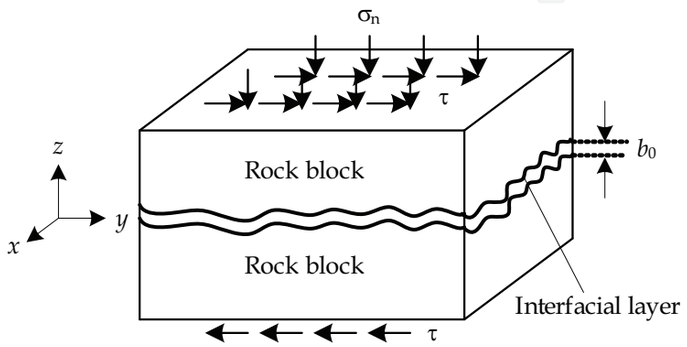

Fig. 3. The interfacial layer model for rock fractures

$$\begin{Bmatrix} \mathrm{d}\sigma_n' \\ \mathrm{d}\tau \end{Bmatrix} = \begin{bmatrix} \lambda+2\mu & 0 \\ 0 & \mu \end{bmatrix} \begin{Bmatrix} \mathrm{d}\varepsilon_n \\ \mathrm{d}\gamma \end{Bmatrix} \tag{1}$$

For convenience, we use u_1 to denote the relative normal displacement of the interfacial layer caused by the effective normal stress σ'_n, δ to denote the relative tangential displacement caused by the shear stress τ, and u_2 to denote the relative normal displacement caused by shear dilation or contraction (positive for dilatant shear, negative for contractive shear). Hence, the total normal relative displacement u is represented as

$$u = u_1 + u_2 \tag{2}$$

The increments of strains, $\mathrm{d}\varepsilon_n$ and $\mathrm{d}\gamma$, can be expressed in terms of the increments of relative displacements, $\mathrm{d}u_1$ and $\mathrm{d}\delta$, as follows:

$$\begin{cases} \mathrm{d}\varepsilon_n = \mathrm{d}u_1 / (b_0 + u) \\ \mathrm{d}\gamma = \mathrm{d}\delta / (b_0 + u) \end{cases} \tag{3}$$

where b_0 is the thickness of the interfacial layer or the initial mechanical aperture of the fracture. Substituting Eq. (3) in Eq. (1) yields:

$$\begin{Bmatrix} \mathrm{d}\sigma_n' \\ \mathrm{d}\tau \end{Bmatrix} = \begin{bmatrix} k_n & 0 \\ 0 & k_s \end{bmatrix} \begin{Bmatrix} \mathrm{d}u_1 \\ \mathrm{d}\delta \end{Bmatrix} \tag{4}$$

where k_n and k_s denote the tangential normal stiffness and tangential shear stiffness of the interfacial layer, respectively.

$$k_n = (\lambda + 2\mu)/(b_0 + u), \quad k_s = \mu/(b_0 + u) \tag{5}$$

Interestingly, k_n and k_s show a hyperbolic relation with normal deformation and characterize the deformation response of the interfacial layer under the idealized conditions that each fracture is replaced by two smooth parallel planar plates connected by two springs with stiffness values k_n and k_s. As can be seen from Eq. (5), as long as the initial normal stiffness and shear stiffness with zero normal displacement, k_{n0} and k_{s0}, are known, they can be used as substitutes for λ and μ.
Substituting Eq. (2) in Eq. (4) results in:

$$\mathrm{d}\sigma_n' = \frac{(\lambda + 2\mu)\mathrm{d}u_1}{b_0 + u_1 + u_2} \tag{6}$$

$$\mathrm{d}\tau = \frac{\mu \mathrm{d}\delta}{b_0 + u_1 + u_2} \tag{7}$$

Suppose normal stress σ_n is firstly applied before the loading of shear stress, u_1 can be obtained by directly integrating Eq. (6):

$$u_1 = (b_0 + u_2)\left[\exp\left(\frac{\sigma_n'}{\lambda + 2\mu}\right) - 1\right] \tag{8}$$

Here, it is to be noted that the elastic constitutive model for the rock fracture leads to an exponential relationship between the fracture closure and the applied normal stress, which has been widely revealed in the literature, e.g., in Min et al. (2004).
On the other hand, the shear expansion caused by $\mathrm{d}\delta$ can be estimated from shear dilation angle d_m:

$$\mathrm{d}u_2 = \tan d_m \, \mathrm{d}\delta \tag{9}$$

By introducing two parameters, s and φ, pertinent to normal stress σ_n, we represent the dilation angle d_m under normal stress σ_n in the form of Barton's strength criterion for joints (Barton, 1976) ($\tau = \sigma_n \tan(2d_m + \varphi_b)$, where φ_b is the basic frictional angle of joints):

$$\tan d_m = \frac{1}{2}\left[\arctan\left(\frac{\tau}{s}\right) - \varphi\right] \tag{10}$$

Obviously, s is a normal stress-like parameter, and φ is a frictional angle-like parameter. But to make the above formulation still valid into pre-dilation state (i.e., shear contraction state), s and φ differ from their initial implications. Later, we will show how they can be back calculated from shear experimental data.
Substituting Eqs. (9) and (10) into (7) yields:

$$\frac{\mathrm{d}u_2}{b_0 + u_1 + u_2} = \frac{1}{2\mu}\left[\arctan\left(\frac{\tau}{s}\right) - \varphi\right]\mathrm{d}\tau \tag{11}$$

By integrating Eq. (11), we have:

$$u_2 = (b_0 + u_1)\left\{\exp\left[\frac{|\tau|}{2\mu}\left(\arctan\frac{|\tau|}{s} - \varphi\right) - \frac{s}{4\mu}\ln\left(1 + \frac{\tau^2}{s^2}\right)\right] - 1\right\} \tag{12}$$

By solving the simultaneous equations, Eqs. (8) and (12), we have:

$$\begin{cases} u_1 = \dfrac{A(1+B)}{1-AB} b_0 \\ u_2 = \dfrac{B(1+A)}{1-AB} b_0 \end{cases} \tag{13}$$

where

$$A = exp\left(\frac{\sigma'_{\mathrm{n}}}{\lambda + 2\mu}\right) - 1 \tag{14}$$

$$B = exp\left[\frac{|\tau|}{2\mu}\left(arctan\frac{|\tau|}{s} - \varphi\right) - \frac{s}{4\mu} ln\left(1 + \frac{\tau^2}{s^2}\right)\right] - 1 \tag{15}$$

Thus, the total normal deformation under normal and shear loading can be obtained,

$$u = u_1 + u_2 = \frac{A + B + 2AB}{1 - AB} b_0 \tag{16}$$

The actual aperture of the fracture, $b = b_0 + u$, is given by:

$$b = b_0 + u = (1 + \chi) b_0 \tag{17}$$

where

$$\chi = \frac{A + B + 2AB}{1 - AB} \tag{18}$$

2.3 Stress-dependent hydraulic conductivity for rock fractures

Since natural fractures have rough walls and asperity areas, it is not appropriate to directly use the aperture derived by Eq. (17) for describing the hydraulic conductivity of the fractures. Instead, an equivalent hydraulic aperture is usually taken to represent the percolation property of the fractures, as demonstrated in Section 1. Based on experimental data, the relationship between the equivalent hydraulic aperture and the mechanical aperture has been widely examined in the literature, and the empirical relations proposed by Lomize (1951), Louis (1971), Patir & Cheng (1978), Barton el al. (1985) and Olsson & Barton (2001) are listed in Table 1. For example, if Patir and Cheng's model is used to estimate the equivalent hydraulic aperture that accounts for the flow-deformation coupling effect in pre-peak shearing stage, then there is

$$b^* = (1 + \chi) b_0 \left[1 - 0.9\exp(-0.56 / C_{\mathrm{v}})\right]^{1/3} \tag{19}$$

where C_v is the variation coefficient of the mechanical aperture of the discontinuities, which is mathematically defined as the ratio of the root mean squared deviation to the arithmetic mean of the aperture. For convenience, Eq. (19) is rewritten as:

$$b^* = b_0 f(\beta) \tag{20}$$

Obviously, $f(\beta)$ is a function of the normal and shear loadings, the mechanical characteristics and the aperture statistics of the fractures.

Thus, the hydraulic conductivity of the fractures subjected to normal and shear loadings is approximated by the hydraulic conductivity of the laminar flow through a pair of smooth parallel plates with infinite dimensions:

$$k = \frac{g b^{*2}}{12\nu} \tag{21}$$

where k is the hydraulic conductivity, g is the gravitational acceleration, and ν is the kinematic viscosity of the fluid.

An alternative approach to account for the deviation of the real fractures from the ideal conditions assumed in the parallel smooth plate theory is to adopt a dimensionless constant, ς, to replace the constant multiplier, 1/12, in Eq. (21), where $0<\varsigma\leq 1/12$ (Oda, 1986). In this manner, the hydraulic conductivity of the fractures is estimated by

$$k = \varsigma \frac{g b^2}{\nu} \tag{22}$$

Clearly, the constant, ς, approaches 1/12 with increasing scale and decreasing roughness of the fractures.

Eqs. (21) and (22) show that the hydraulic conductivity of a rock fracture varies quadratically with its mechanical aperture. The latter depends, by Eq. (18), on the normal and shear stresses applied on the fracture. Hence, we call the established model, Eq. (21) or (22), the stress-dependent hydraulic conductivity model, and it is suitable to describe the hydraulic behaviour of the fractures subjected to mechanical loading in the pre-peak stage.

Authors	Expressions	Descriptions
Lomize (1951)	$b^* = b\left[1.0 + 6.0(e/b)^{1.5}\right]^{-1/3}$	b^* is the equivalent hydraulic aperture of fractures, b the mechanical aperture, e the absolute asperity height, e_m the average asperity height, D_H the hydraulic radius, C_v the variation coefficient of the mechanical aperture, JRC the joint roughness coefficient, JRC_0 the initial value of JRC, JRC_{mob} the mobilized JRC, δ the shear displacement and δ_p the peak shear displacement.
Louis (1971)	$b^* = b\left[1.0 + 8.8(e_m/D_H)^{1.5}\right]^{-1/3}$	
Patir & Cheng (1978)	$b^* = b\left[1 - 0.9\exp(-0.56/C_v)\right]^{1/3}$	
Barton, et al. (1985)	$b^* = b^2 JRC^{-2.5}$	
Olsson & Barton (2001)	$\begin{cases} b^* = b^2 JRC_0^{-2.5} & \delta \leq 0.75\delta_p \\ b^* = b^{1/2} JRC_{mob} & \delta \geq \delta_p \end{cases}$	

Table 1. Empirical relations between equivalent hydraulic aperture and mechanical aperture

2.4 Validation of the elastic constitutive model

The key point of the stress-dependent hydraulic conductivity model is whether the established elastic constitutive model can properly describe the variation of mechanical aperture under normal and shear loadings at low stress level. Here, we use the results of the laboratory test performed by Liu et al. (2002) to validate the mechanical model. The test was conducted to study shear-flow coupling properties for a marble fracture with fillings of sand under low normal stresses and small shear displacements.

The marble specimen for shear-flow coupling test is illustrated in Fig. 4, which was collected from the Daye Iron Mine in China. The uniaxial compressive strength and density of the rock sample are 52.4 MPa and 2.66×10^3 kg/m^3, respectively. The specimen was cut into round shape and the fracture surfaces were polished, with its size of 290 mm in diameter and 200 mm in height. The opposite walls of the fracture were cemented with a layer of filtered sands with their diameters ranged from 0.5 to 0.69 mm, and the fracture was further filled with the same sands. The initial aperture of the fracture, b_0, is about 1.31 mm.

The coupled shear-flow test were conducted by first applying a prescribed normal stress ranging between 0.1 and 0.5 MPa and then applying shear displacement in steps until a maximum displacement of about 0.4 mm was reached. During tests, steady-state fluid flow rate and normal displacement were continuously recorded.

With such low normal stresses and small shear displacements, it is reasonable to consider that the fracture behaves elastic during the coupled shear-flow test. According to the experimental results, the elastic parameters, λ and μ, of the fracture with fillings are estimated as λ=1.81 MPa and μ=3.62 MPa. In order to enable Eq. (16) to predict the mechanical aperture of the facture under normal and shear loads, the normal stress-like parameter, s, and the frictional angle-like parameter, φ, should be further determined. Fortunately, both of them can be derived by fitting the experimental curve between normal displacement and shear displacement, as plotted in Fig. 5, using Eq. (16) such that the least square error is minimized. With this approach, we obtain that for σ_n=0.1 MPa, s=0.062, φ=1.324, and for σ_n=0.4 MPa, s=0.046, φ=1.310.

Fig. 5 plots the experimental results as well as the model predictions of the relation between mechanical aperture and shear displacement of the fracture under constant normal stresses. Generally, the proposed elastic constitutive model manifests the behaviour of the fracture with fillings during the shear-flow coupling test with low normal and shear loads. Shear contraction is observed in the initial 0.06-0.08 mm of shear displacement, which is followed by shear dilation in the remaining of the shear displacement. This property, which is actually ensured by the empirical relation assumed in Eq. (9), suggests that the resultant model is suitable for phenomenologically describing the pre-peak shear-flow coupling effect of fractures.

Fig. 6 further depicts the sensitivity of s and φ on the behaviour of the fracture. In Fig. 6(a), φ is fixed to 1.324, while s varies from 0.02 to 0.08. As s increases, shear contraction more apparently manifests, and the mechanical aperture versus shear displacement curves become lower as a whole. On the other hand, the effect of varying φ from 0.524 to 1.222 but fixing s to 0.062 is plotted in Fig. 6(b). For small value of φ, shear contraction is trivial and the curve extends with a larger slope. As φ increases, however, shear contraction becomes relatively remarkable and the curve turns relatively flat. Thus, by adjusting s and φ, the mechanical and hydraulic behaviours of the fracture can be appropriately established.

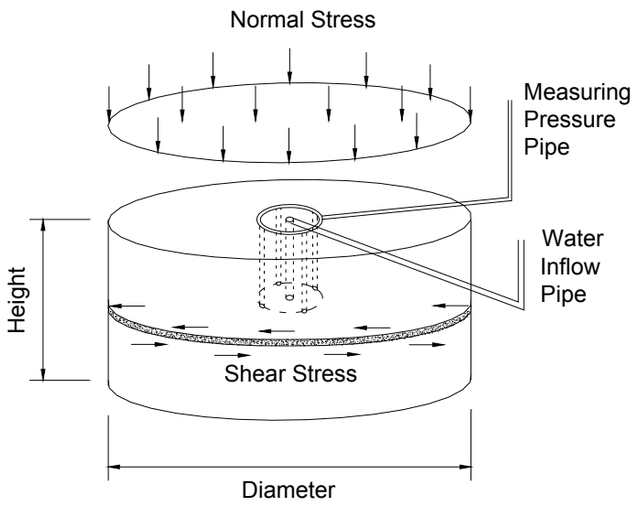

Fig. 4. Sketch of the marble specimen for shear-flow coupling test

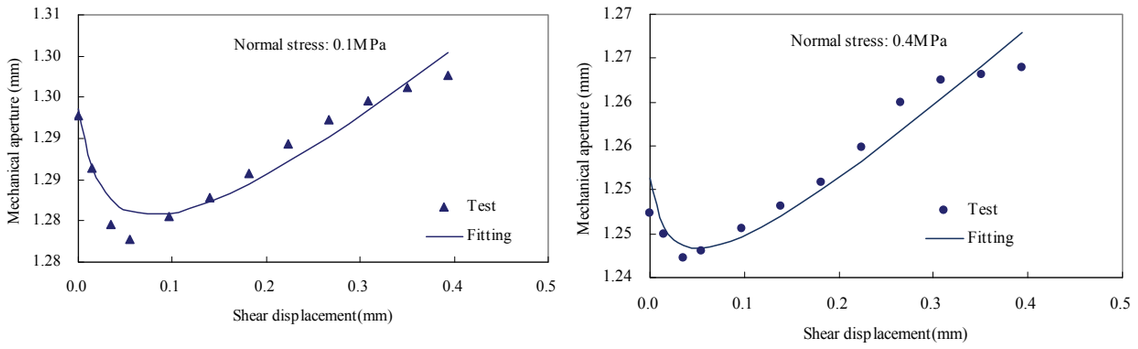

(a) (b)

Fig. 5. Mechanical aperture versus shear displacement curve under constant normal stress: (a) Normal stress: 0.1 MPa and (b) Normal stress: 0.4 MPa.

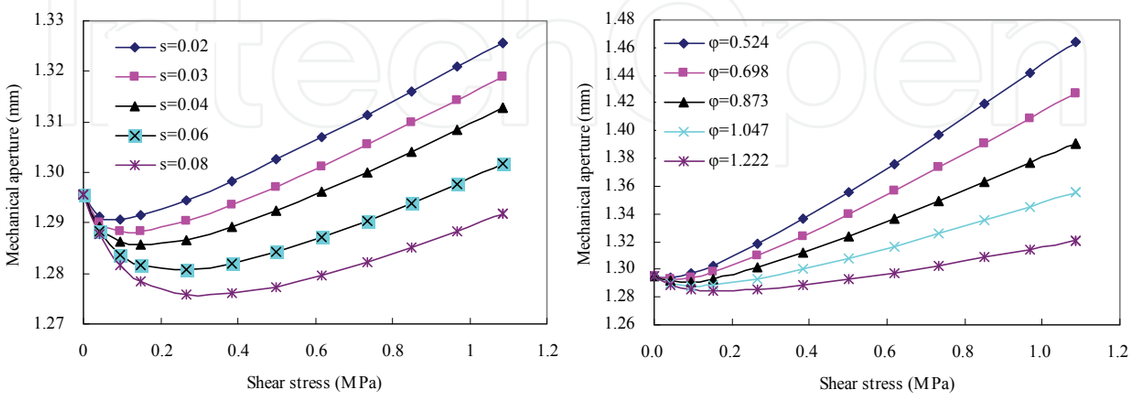

(a) (b)

Fig. 6. The sensitivity of s and φ on the behavior of the fracture: (a) φ=1.324 and (b) s=0.062

3. Strain-dependent hydraulic conductivity of rock fractures

In this section, we develop an elasto-plastic constitutive model for single hard rock fractures with consideration of nonlinear normal deformation and post-peak shear dilatancy, and then formulate the strain-dependent hydraulic conductivity for the fractures under dilated shear loading. Compared with the stress-dependent model presented in Section 2, one major difference is that the strain-dependent model is capable of describing the influence of post-peak mechanical response on the hydraulic properties of the fractures. This work is of paramount importance in the sense that the theoretical results are directly comparable with the experimental data of coupled shear-flow test, e.g. in Esaki et al. (1999). The strain-dependent hydraulic conductivity tensor can then be developed on this basis, which will be presented later in Section 5.

3.1 An elasto-plastic constitutive model for rock fractures

The underlying physical model considered is the same with the model plotted in Fig. 3, in which a fracture of hard rock is located at the mid-height of a specimen between two intact rock blocks. The height of the specimen is denoted by s, and the initial aperture of the fracture is b_0. When constant normal stress σ_n and increasing shear displacement δ are applied on the specimen, typical and idealized curves of shear displacement versus shear stress and shear displacement versus normal displacement (i.e. $\delta \sim \tau$ curve and $\delta \sim u$ curve) are plotted in Fig. 7. The shear stress increases linearly with the shear displacement (linked by the initial shear stiffness of the fracture, k_{s0}) until the shear stress approaches the peak, τ_p, which is then followed by a shear softening process in which the shear stress decreases to a residual level at a decreasing gradient with increasing shear displacement. For the purpose of deriving the hydraulic property of the fracture in post-peak loading section, however, an elastic-perfectly plastic $\delta \sim \tau$ relationship can be assumed, as shown in Fig. 7(a).

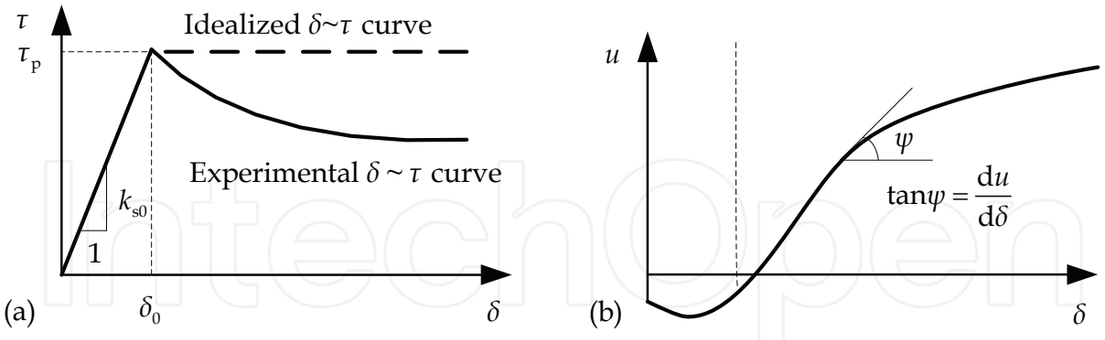

Fig. 7. Typical and idealized curves of shear displacement versus shear stress and shear displacement versus normal displacement of a fracture subjected to normal and shear loads

The deformation response of a rock fracture subjected to normal and shear loadings includes two components: one is the nonlinear closure of the fracture due to normal compression, and the other is the opening of the fracture due to shear dilation. Experimental results in Esaki et al. (1999) show that in the shearing process under constant normal loading, dilatancy will start when the shear stress approaches the peak and it increases at a decreasing gradient with increasing shear displacement, as illustrated in Fig. 7(b). As a result, the aperture of the fracture and then the hydraulic conductivity vary with increasing shear displacement.

Therefore, we may consider that shear dilatancy as well as the change in hydraulic conductivity accompanies normal and plastic shear deformations of the fracture. To deduce the hydraulic conductivity of the fracture with an averaging method, which will be further used later for deriving the hydraulic conductivity tensor for fractured rocks, we view the specimen with fracture as an equivalent continuous medium, i.e. the hydromechanical properties of the fracture are averaged into the whole specimen. As can be seen later, such a treatment does not affect our final solution to a single fracture, but it renders valid the small strain assumption on the fractures in the presence of post-sliding plasticity.

For a one-dimensional problem with a single rock fracture, the elasto-plastic constitutive model can be represented in the following forms:

$$\gamma_{\mathrm{p}} = \gamma - \gamma_{\mathrm{e}} = \frac{\delta}{s} - \frac{\delta_0}{s} = \frac{\delta}{s} - \frac{\tau_{\mathrm{p}}}{s k_{\mathrm{s0}}} \tag{23}$$

$$\varepsilon_{\mathrm{n}} = \frac{\sigma'_{\mathrm{n}}}{s k_{\mathrm{n}}} + \int \tan\psi \, \mathrm{d}\gamma_{\mathrm{p}} \tag{24}$$

where γ, γ_{e} and γ_{p} are the total shear strain, the elastic shear strain and the plastic shear strain of the fracture, respectively; ε_{n} is the normal strain of the fracture; τ_{p} is the peak shear stress of the fracture under effective normal stress σ'_{n}; k_{n} and k_{s0} are, respectively, the normal stiffness and the initial shear stiffness of the fracture; δ_0 is the maximum elastic shear displacement upon shear yielding, with $\delta_0 = \tau_{\mathrm{p}}/k_{\mathrm{s0}}$, as shown in Fig. 7(a); and ψ is the mobilized dilatancy angle of the fracture. Note that in Eq. (24), the first term on the right hand side denotes the nonlinear closure of the fracture subjected to effective normal stress σ'_{n}, while the second term denotes the opening of the fracture due to shear dilatancy.

Existing studies have indicated that shear dilatancy is highly dependent on the plasticity already experienced by the fractures and normal stress, and non-negligibly dependent on scale (Barton & Bandis, 1982; Yuan & Harrison, 2004; Alejano & Alonso, 2005). The decaying process of the dilatancy angle in line with plasticity can be described by the following negative exponential expression through the plastic shear strain, γ_{p}, or indirectly through the plastic shear displacement, δ, on the basis of Eq. (23):

$$\psi = \psi_{\mathrm{peak}} \exp\left[-r(\delta - \delta_0)\right] \tag{25}$$

where r is a parameter for modelling the rate of decay that ψ undergoes as the plastic shear strain evolves. If r=0, then a constant dilatancy angle is recovered. As $r \to \infty$, the dilatancy angle quickly decays to zero. ψ_{peak} is the peak dilatancy angle of the fracture in the form of (Barton & Bandis, 1982)

$$\psi_{\mathrm{peak}} = JRC \cdot \log_{10} \frac{JCS}{-\sigma'_{\mathrm{n}}} \tag{26}$$

where JRC and JCS are the roughness coefficient and the wall compressive strength of fractures, respectively, and the actual values of them should be scale-corrected (Barton & Bandis, 1982). Thus, the dependencies of fracture dilatancy on plasticity, normal stress and scale are established through Eqs. (25) and (26).

Note that Eq. (25) shares the same shape with the asperity angle proposed for the description of shear dilatancy and surface degradation (Plesha, 1987), but the latter is represented as a function of the plastic tangential work. With the assumption of elastic-perfectly plasticity, they are fully equivalent for monotonic loading (Jing et al., 1993). Cyclic loading is not a concern in this simple model, but when cyclic loading is involved, another independent function can be associated to the reverse loading that starts from the original point, just as the suggestion given in Plesha (1987) for asperity angles in two opposite directions, in order to satisfy the thermodynamic restriction condition presented in Jing et al. (1993).

Using the Mohr-Coulomb criteria, the peak shear stress τ_{p} of the fracture under effective normal stress σ'_{n} satisfies

$$\tau_{\mathrm{p}} = -\sigma'_{\mathrm{n}} \tan\varphi + c \tag{27}$$

where φ and c are the frictional angle and the cohesion of the fracture.

Differentiating Eq. (23) yields

$$\mathrm{d}\gamma_{\mathrm{p}} = \mathrm{d}\gamma = \frac{1}{s}\mathrm{d}\delta \tag{28}$$

Combining Eqs. (24) and (28) results in

$$\Delta b \approx s\varepsilon_{\mathrm{n}} = \frac{\sigma'_{\mathrm{n}}}{k_{\mathrm{n}}} + \int_{\delta_0}^{\delta} \tan\psi(\delta)\mathrm{d}\delta \tag{29}$$

An interesting phenomenon in Eq. (29) is, as described before, the change in the aperture of the fracture, Δb, is irrelevant to the height of the specimen, s. To conveniently use this formulation, two remedies can be further made:

First, suppose that the hyperbolic variation of k_{n} with the increase of aperture can be considered in the following (Huang et al., 2002):

$$k_{\mathrm{n}} = \frac{-\sigma'_{\mathrm{n}} + b_0 k_{\mathrm{n0}}}{b_0} \tag{30}$$

where k_{n0} is the initial normal stiffness of the fracture.

Second, by employing the Taylor series expansion (truncated at the third order term), $\tan\psi$ can be adequately approximated by $\psi + \psi^3/3$ in radians for a rather large ψ_{peak}, e.g. 30°.

From Eq. (29) and the above two remedies, we have

$$\Delta b = \chi b_0 \tag{31}$$

$$b = b_0 + \Delta b = (1 + \chi) b_0 \tag{32}$$

with the parameter, χ, in the following form

$$\chi = \frac{\sigma'_{\mathrm{n}}}{-\sigma'_{\mathrm{n}} + b_0 k_{\mathrm{n0}}} + \frac{1}{b_0}\left\{\frac{\psi_{\mathrm{peak}}}{r}\left[1 - \mathrm{e}^{-r(\delta-\delta_0)}\right] + \frac{\psi_{\mathrm{peak}}^3}{9r}\left[1 - \mathrm{e}^{-3r(\delta-\delta_0)}\right]\right\} \tag{33}$$

3.2 Strain-dependent hydraulic conductivity for rock fractures

Rewrite from Eq. (22) the initial hydraulic conductivity of the fracture, k_0, in the following form:

$$k_0 = \varsigma \frac{g b_0^2}{\nu} \tag{34}$$

Then, the hydraulic conductivity of the fracture under effective normal stress σ'_n and shear displacement δ can be described by

$$k = \varsigma \frac{g b^2}{\nu} = k_0 (1 + \chi)^2 \tag{35}$$

Hence, a theoretical model of the hydraulic conductivity for a single rock fracture is finally formulated, which is totally determined by the effective normal stress σ'_n and the shear displacement δ, as well as a set of parameters characterizing the behaviour of the fracture (i.e. b_0, ς, k_{n0}, k_{s0}, φ, c, *JRC*, *JCS* and r, which all can be deduced or back-calculated from experimental data).

Note that by Eqs. (35) and (33), the proposed hydraulic conductivity model for rock fractures subjected to normal and shear loadings with mobilized dilatancy behaviour depends in form on the plastic shear displacement, but from Eq. (23), one observes that the model depends indirectly on the plastic shear strain. Thus, we classify the established model into the stain-dependent hydraulic conductivity model.

3.3 Validation of the proposed model

Esaki et al. (1999) systematically investigated the coupled effect of shear deformation and dilatancy on hydraulic conductivity of rock fractures by developing a new laboratory technique for coupled shear-flow tests of rock fractures. In this section, we validate the theory proposed in Section 3.2 using the experimental data reported in Esaki et al. (1999). For this purpose, we first briefly introduce the experiments, and then predict our analytical results through Eqs. (31) and (35) by directly comparing with the experimental data.

3.3.1 The coupled shear-flow tests

The coupled shear-flow tests were conducted with an artificially created granite fracture sample under various constant normal loads and up to a residual shear displacement of 20 mm (Esaki et al., 1999). The underlying specimen for coupled shear-flow tests is sketched in Fig. 3, with its size of 120 mm in length, 100 mm in width and 80 mm in height. The initial aperture of the created fracture, b_0, is about 0.15 mm. The value of *JRC* is 9, and the value of *JCS* is 162 MPa, respectively.

The coupled shear-flow tests were conducted by first applying a prescribed normal stress ranging between 1 MPa and 20 MPa and then applying shear displacement in steps at a rate of 0.1 mm/s until a maximum shear displacement of 20 mm was reached. During tests, steady-state fluid flow rate, shear loading and dilatancy were all continuously recorded. The hydraulic aperture and conductivity were back-calculated by applying the cubic law, with the flow equations solved by using a finite difference method.

3.3.2 Determination of the parameters for the proposed model

Some of the experimental values of the mechanical parameters of the fracture specimen during the coupled shear-flow tests are listed in Table 2 (taken from Table 1 in Esaki et al. (1999)). Using the data as listed in Table 2, we plot the peak shear stress versus normal stress curve in Fig. 8, which can be fitted by a linear equation $\tau_p=1.058\sigma_n+0.993$ with a high correlation coefficient of 0.9999. Therefore, the shear strength of the specimen can be derived as $\varphi=46.6°$ and $c=0.99$ MPa, respectively.

σ_n (MPa)	τ_p (MPa)	k_{s0} (MPa/mm)
1	2.06	3.37
5	6.16	10.65
10	11.74	11.97
20	22.10	17.97

Table 2. Mechanical parameters of the artificial fracture (After Esaki et al. (1999))

The initial normal stiffness of the fracture of the specimen, k_{n0}, has to be estimated from the recorded initial normal displacement with zero shear displacement under different normal stresses. From the data plotted in Fig. 9 (which is taken from Fig. 7b in Esaki et al. (1999)), k_{n0} can be estimated as $k_{n0}=100$ MPa/mm by considering the possible deformation of the intact rock under high normal stresses. It is to be noted that in the remainder of this section, the hard intact rock deformation of the small specimen is neglected, meaning that the normal displacement of the specimen mainly occurs in the fracture of the specimen and it is approximately equal to the increment of the mechanical aperture of the fracture.

Theoretically, the decay coefficient of the fracture dilatancy angle, r, can be directly measured from the normal displacement versus shear displacement curves as plotted in Fig. 9. A better alternative, however, is to fit the experimental curves using Eq. (31) such that the least square error is minimized. By this approach, we obtain that $r=0.13$ with a correlation coefficient of 0.9538.

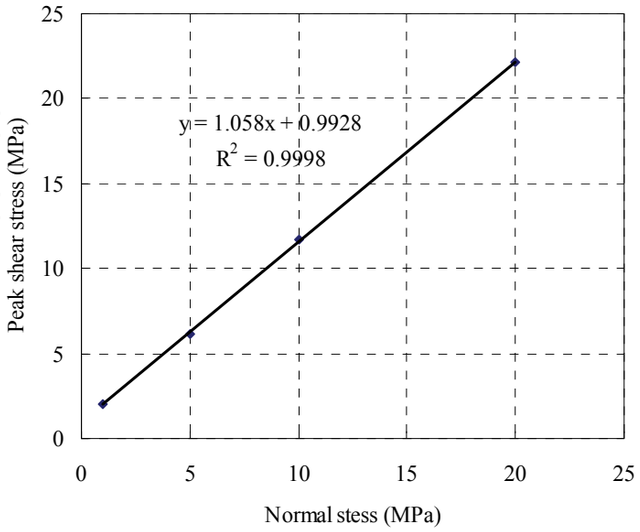

Fig. 8. Peak shear stress versus normal stress curve of the fracture.

To obtain the dimensionless constant, ς, in Eq. (35) that relates the mechanical aperture to the hydraulic conductivity of the fracture under testing, further efforts are needed. A simple approach is to back-calculate ς directly using Eq. (34) with initial hydraulic conductivity, k_0. But similarly, the better alternative is to fit the hydraulic conductivity versus shear displacement curves, as plotted in Fig. 11 (which is taken from Fig. 7c-f in Esaki et al. (1999)), using Eq. (35) such that the least square error is minimized. With such a method, we obtain that ς=0.00875. This means that the mechanical aperture, b, and the hydraulic aperture, b^*, are linked with b^*=0.324b, which is very close to the experimental result shown in Fig. 8 in Esaki et al. (1999).

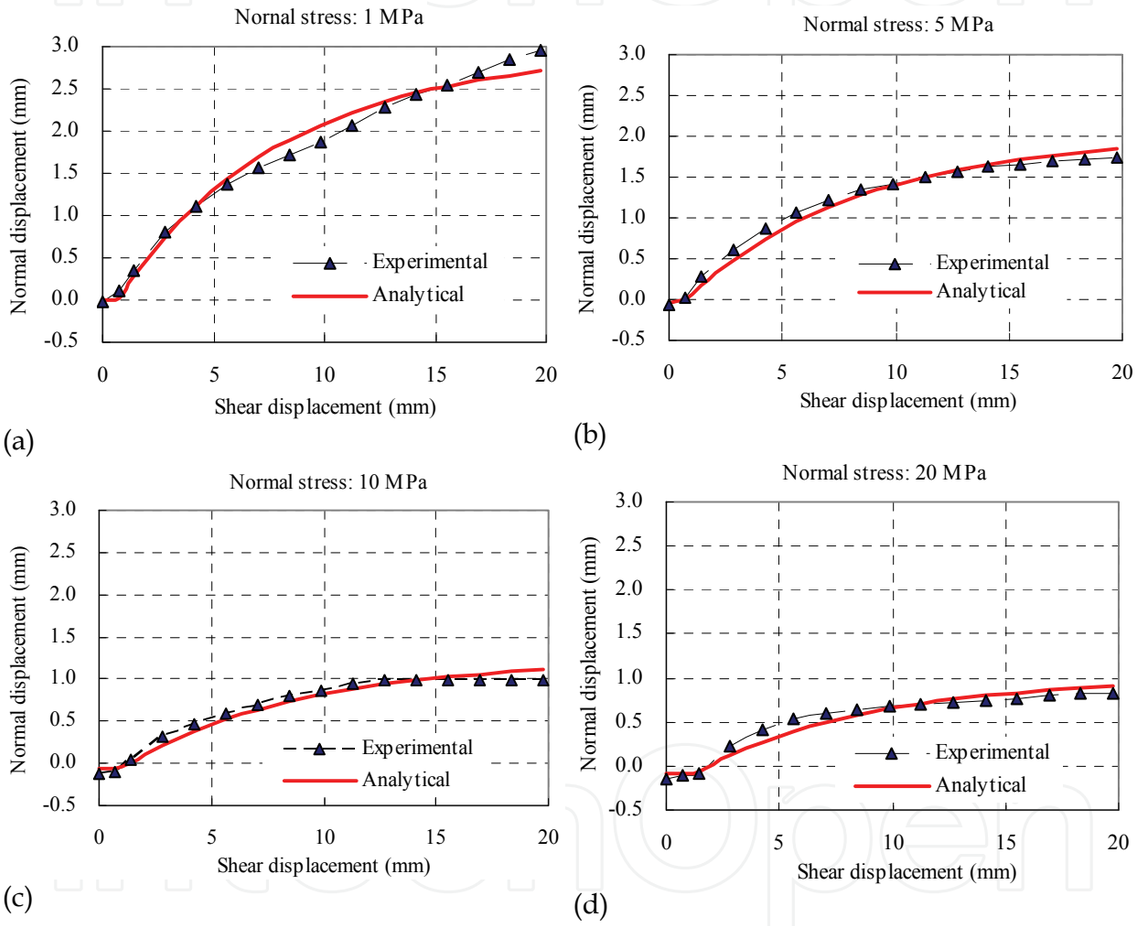

Fig. 9. Comparison of the fracture aperture analytically predicted by Eq. (31) with that measured in coupled shear-flow tests.

3.3.3 Validation of the proposed theory

With the necessary parameters obtained in Section 3.3.2, we are now ready to compare the proposed model in Eqs. (31) and (35) with the experimental data presented in Esaki et al. (1999). Note that although the experimental data are available for one cycle of forward and reverse shearing, only the results for the forward shearing part are considered. The reverse shearing process, however, can be similarly modelled.

Fig. 9 depicts the relations between the mechanical aperture and shear displacement that were measured from the coupled shear-flow tests presented in Esaki et al. (1999) and predicted by using the proposed model given in Eq. (31) under different normal stresses applied during the testing. It can be observed from Fig. 9 that our proposed analytical model is able to describe the shear dilatancy behaviour of a real fracture under wide range of normal stresses between 1 MPa and 20 MPa by feeding appropriate parameters. Even the fracture aperture increases by one order of magnitude due to shear dilation, the analytical model still fitted the experimental results well. For practical uses, the slight discrepancies between the analytical results and the experimental data are negligible and the proposed model is accurate enough to characterize the significant dilatancy behaviour of a real fracture.

This performance is largely attributed to the dilatancy model introduced through Eqs. (25) and (26). The dilatancy angles of the fracture evolving with the plastic shear displacement under different normal stresses are illustrated in Fig. 10. The high dependencies of the dilatancy angle of the fracture on normal stress and plasticity are clearly demonstrated in the curves. The peak dilatancy angle, which can be rather accurately modelled by Barton's peak dilatancy relation (Barton & Bandis, 1982), decreases logarithmically with the increase of the applied normal stress. For normal stresses of 1 MPa, 5 MPa, 10 MPa and 20 MPa, the peak dilatancy angles are 19.9°, 13.6°, 10.9° and 8.2°, respectively. On the other hand, the dilatancy angle undergoes negative exponential decay with increasing plastic shear displacement, a process related to surface degradation of rough fractures.

Fig. 11 shows the hydraulic conductivity versus shear displacement relations that were back-calculated from fluid flow results using the finite difference method from the coupled shear-flow tests presented in Esaki et al. (1999) and that are predicted by the proposed model given in Eq. (35) under different normal stresses during testing. As shown in the semi-logarithmic graphs in Fig. 11, the proposed analytical model can well predict the evolution of hydraulic conductivity of the tested rock fracture, with the change in the magnitude of 2 orders, during coupled shear-flow tests under different normal stresses. The ratios of the predicted hydraulic conductivities to the corresponding experimental results all fall in between 0.3 and 3.0, indicating that they are rather close in orders of magnitude and the predicted results are suitable for practical use.

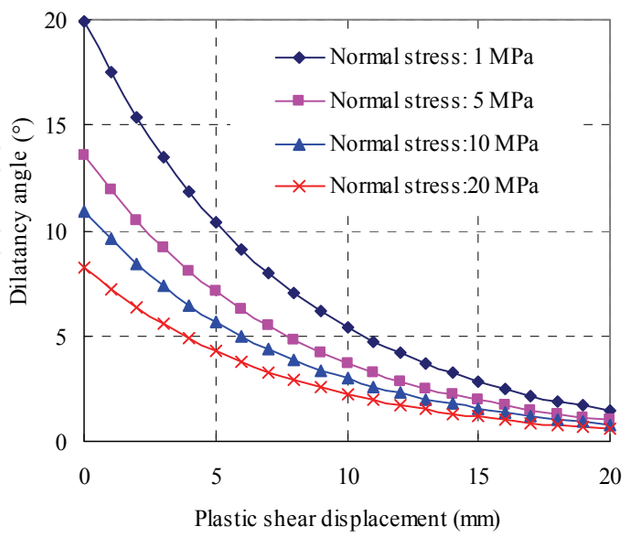

Fig. 10. Dilatancy angles of the fracture evolving with the plastic shear displacement under different normal stresses.

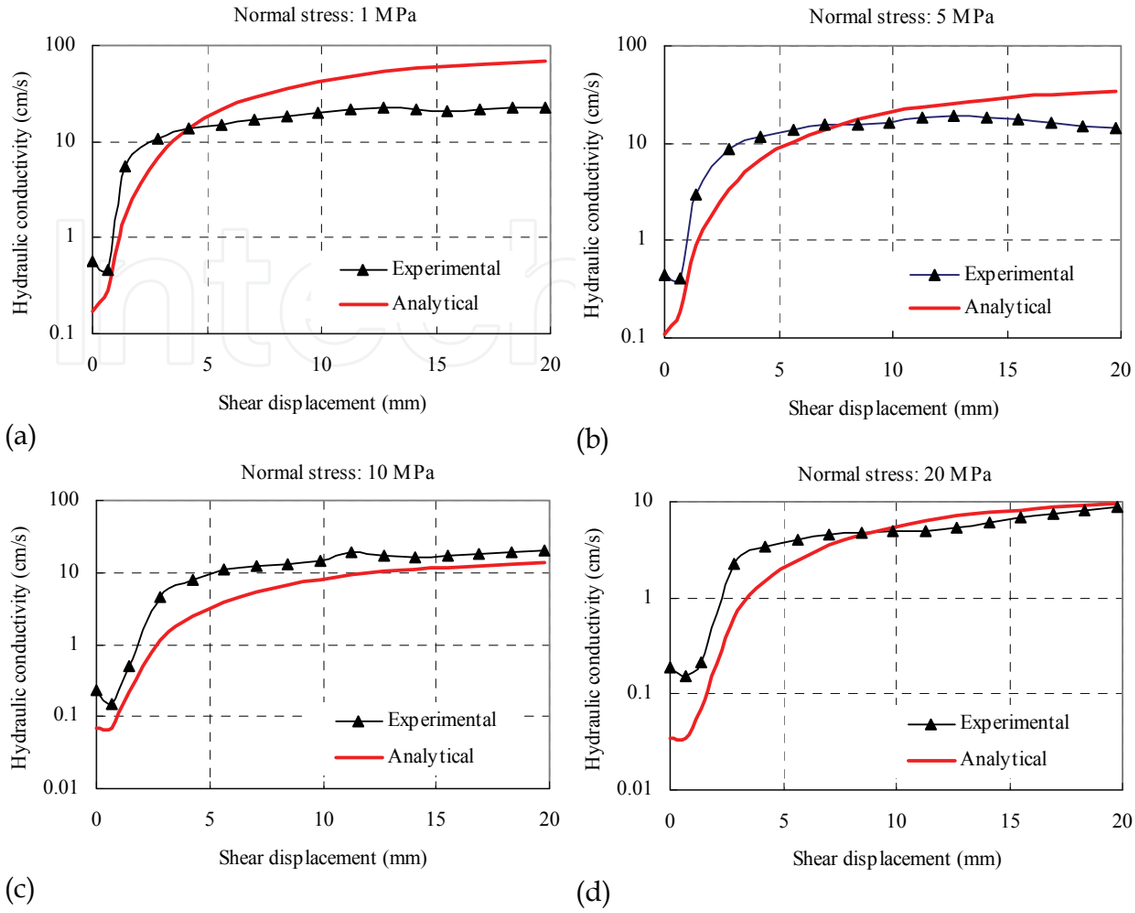

Fig. 11. Comparison of the hydraulic conductivity analytically predicted by Eq. (35) with that calculated from coupled shear-flow tests with finite difference method.

4. Stress-dependent hydraulic conductivity tensor of fractured rocks

When the response of each fracture under normal and shear loading is understood (see Section 2), the remaining problem is how to formulate the hydraulic conductivity for fractured rock mass based on the geometry of the underlying fracture network. Fig. 12 depicts a two-dimensional fracture network (taken after Min et al. (2004)) in a biaxial stress field. As shown in Fig. 12, each fracture plays a role in the hydraulic conductivity of the rock mass, and its contribution primarily depends on its stress state, its occurrence, as well as its connectivity with other fractures. Also shown in Fig. 12 is the scale effect of the rock mass on hydraulic properties. When the size of the rock mass is small, only a few number of fractures are included and heterogeneity of the hydraulic conductivity of the rock mass may dominate. As the population of factures grows with the increasing size, an upscaling scheme may be available to derive a representative hydraulic conductivity tensor for the rock mass at the macroscopic scale.

Based on the above observations, in this section, we formulate an equivalent hydraulic conductivity tensor for fractured rock mass based on the superposition principle of liquid dissipation energy, in which the concept of *REV* is integrated and the applicability of an equivalent continuum approach is able to be validated.

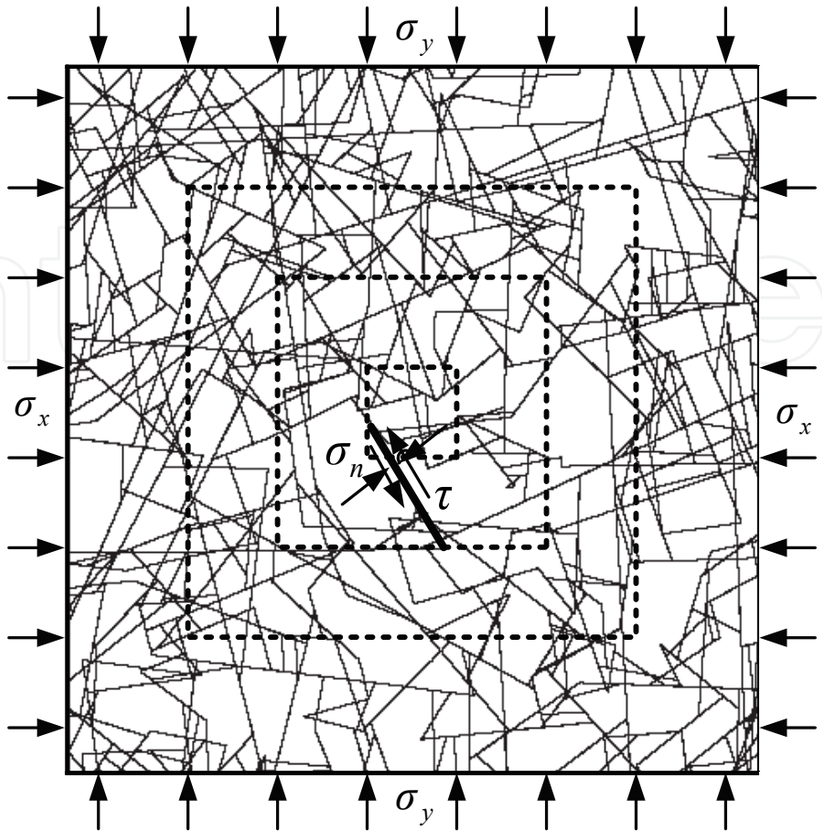

Fig. 12. A fracture network (taken after Min et al. (2004)) in biaxial stress field and the scale effect of the rock mass

4.1 Computational model

Without loss of generality, the global coordinate system $X_1X_2X_3$ is established in such a way that its X_1-axis points towards the East, X_2-axis toward the North and X_3-axis vertically upward. A local coordinate system $x_1^f x_2^f x_3^f$ is associated with the fth set of fractures such that the x_1^f -axis is along the main dip direction, the x_2^f -axis is in the strike, and the x_3^f -axis is normal to the fractures, as shown in Fig. 13.

In order to formulate the stress-dependent hydraulic conductivity tensor for fractured rock masses using the aforementioned elastic constitutive model for rock fractures, the following assumptions, similar to Oda (1986), are made in this section:

1. A cube of volume, V_p, is considered as the flow region of interest, which is cut by n sets of fractures. The orientation of each set of fractures is indicated by a mean azimuth angle β and a mean dip angle α. Other geometrical statistics of the fractures are assumed to be available through field measurements or empirical estimations.
2. Even though the geometry of real fractures is complex, generally it can be simplified as a thin interfacial layer with radius r and aperture b^*.
3. The rock mass is regarded as an equivalent continuum medium, which means the representative elementary volume (REV) exists in the rock mass and its size is smaller than or equal to V_p.

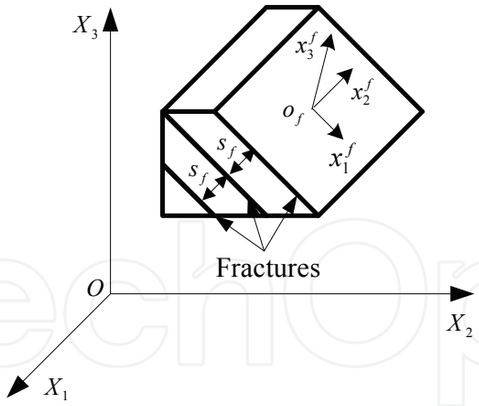

Fig. 13. Coordinate systems

4.2 Stress-dependent hydraulic conductivity tensor

Fluid flow through the equivalent continuum media can be described by the generalized 3-D Darcy's law as follows:

$$v = \mathbf{KJ} \tag{36}$$

where v denotes the vector of flow velocities, $\mathbf{J}$ denotes the vector of hydraulic gradients, and $\mathbf{K}$ is the hydraulic conductivity tensor for the rock mass.

For steady-state seepage flow, the dissipation energy density, $e(X_1, X_2, X_3)$, of fluid flow through the media can be represented as (Indelman & Dagan, 1993):

$$e = \frac{1}{2}\mathbf{J}^{\mathrm{T}}\mathbf{KJ} \tag{37}$$

Hence, the total flow dissipation energy, E, in the rock mass V_{p} can be calculated by performing an integration throughout the whole flow domain:

$$E = \int_{V_{\mathrm{p}}} e\mathrm{d}\Omega = \frac{1}{2}\int_{V_{\mathrm{p}}} \mathbf{J}^{\mathrm{T}}\mathbf{KJ}\mathrm{d}\Omega \tag{38}$$

If REV does exist in the rock mass and its size is smaller than or equal to V_{p}, by defining $\bar{\mathbf{J}}$ to be the vector of the average hydraulic gradient within V_{p} and $\bar{\mathbf{K}}$ to be the average hydraulic conductivity tensor, Eq. (38) can be reduced to:

$$E = \frac{1}{2}\bar{\mathbf{J}}^{\mathrm{T}}\bar{\mathbf{K}}\bar{\mathbf{J}}V_{\mathrm{p}} \tag{39}$$

Suppose that the volume density of the ith set of fractures is J_{vi}. The number of this set of fractures can be estimated by $m_i = J_{vi}\, V_{\mathrm{p}}$.

For permeable rock matrix, the flow dissipation energy shown in Eq. (39) consists of two components, i.e., the flow dissipation energy through rock matrix, E_{r}, and the flow dissipation energy through crack network, E_{c}:

$$E = E_{\mathrm{r}} + E_{\mathrm{c}} \tag{40}$$

E_r can be represented as:

$$E_r = \frac{1}{2}\bar{\mathbf{J}}^T \bar{\mathbf{K}}_r \bar{\mathbf{J}} V_p \tag{41}$$

where $\bar{\mathbf{K}}_r$ denotes the hydraulic conductivity tensor for rock matrix. If rock matrix is impermeable, all elements in $\bar{\mathbf{K}}_r$ vanish.

To estimate E_c, we introduce a weight coefficient W_{ij} to describe the effect of the connectivity of the fracture network on fluid flow:

$$W_{ij} = \xi_{ij} / \bar{\xi}_i \tag{42}$$

where ξ_{ij} is a stochastic variable denoting the number of fractures intersected by the jth fracture belonging to the ith set; and $\bar{\xi}_i$ denotes the maximum number of fractures cut by the ith set of fractures. Obviously, $0 \le W_{ij} \le 1$ and when $\xi_{ij} = 0$, $W_{ij} = 0$. This implies that an entirely isolated fracture which does not intersect any other fracture effectively contributes nothing to the hydraulic conductivity of the total rock mass.

For the jth fracture belonging to the ith set, a void volume equal to $\pi r_{ij}^2 b_{ij}^*$ is associated with it. Then, the flow dissipation energy through it is described as:

$$E_{cij} = W_{ij} e_{ij} \pi r_{ij}^2 b_{ij}^* \tag{43}$$

where e_{ij} is shown as follows:

$$e_{ij} = \frac{1}{2} k_{ij} \bar{\mathbf{J}}_{ci}^T \bar{\mathbf{J}}_{ci} \tag{44}$$

where k_{ij} denotes the hydraulic conductivity of the jth fracture of the ith set, which can be calculated by the stress-dependent hydraulic conductivity model, Eq. (21).

$\bar{\mathbf{J}}_{ci}$ denotes the hydraulic gradient within the ith set of fractures:

$$\bar{\mathbf{J}}_{ci} = (\boldsymbol{\delta} - \mathbf{n}_i \otimes \mathbf{n}_i)\bar{\mathbf{J}} \tag{45}$$

where $\boldsymbol{\delta}$ is the Kronecker delta tensor, and $\boldsymbol{n}_i$ denotes the unit vector normal to the ith set of fractures, with its components $n_1=\sin\alpha\sin\beta$, $n_2=\sin\alpha\cos\beta$, and $n_3=\cos\alpha$.

Thus, E_c can be represented as

$$E_c = \frac{g\pi}{12\nu} \sum_{i=1}^{n} \sum_{j=1}^{m_i} W_{ij} r_{ij}^2 b_{ij}^{*3} \bar{\mathbf{J}}^T (\boldsymbol{\delta} - \mathbf{n}_i \otimes \mathbf{n}_i) \bar{\mathbf{J}} \tag{46}$$

From Eqs. (39)-(41), (46) and (20), it can be referred that

$$\bar{\mathbf{K}} = \bar{\mathbf{K}}_r + \frac{g\pi}{12\nu V_p} \sum_{i=1}^{n} \sum_{j=1}^{m_i} W_{ij} f^3(\beta_{ij}) r_{ij}^2 b_{0ij}^3 (\boldsymbol{\delta} - \mathbf{n}_i \otimes \mathbf{n}_i) \tag{47}$$

In Eq. (47), $\boldsymbol{n}$ is determined by the orientation of the fractures, which reflects the effect of the orientation of the fractures on the fluid flow. r and b_0 represent the size or the scale of the

fractures; they retrain the fluid flow through the fractures from their developing magnitude. W is a parameter introduced to show the impact of the connectivity of the fracture network on fluid flow. Finally, $f(\beta)$ is a function used to demonstrate the coupling effect between fluid flow and stress state.

The hydraulic tensor for fractured rock masses given in Eq. (47) is related to the volume of the flow region, V_p, which exactly shows the size effect of the hydraulic properties. Intuitively, the smaller the V_p size is, the less number of fractures is contained within the volume, and thus the poorer the representative of the computed hydraulic conductivity tensor. On the other hand, when V_p is increased up to a certain value, the fractures involved in the cubic volume are dense enough and the hydraulic conductivity tensor for the rock mass does not vary with the size of the volume. This V_p size is exactly the representative elementary volume, *REV*, of the flow region. The V_p size of the flow region is required to be larger than *REV* for estimating the hydraulic conductivity tensor for the fractured rock mass. Otherwise, treating the fractured rock mass as an equivalent continuum medium is not appropriate, and the discrete fracture flow approach is preferable.

4.3 Comparison with Snow's and Oda's models

Now we make a comparison between the formulation of the hydraulic conductivity tensor presented in Eq. (47) and the formulation given by Snow (1969) as well as the formulation given by Oda (1986). The Snow's formulation is as follows:

$$\mathbf{K} = \frac{g}{12\nu}\sum_{i=1}^{n}\frac{b_i^3}{s_i}\left(\boldsymbol{\delta} - \mathbf{n}_i \otimes \mathbf{n}_i\right) \tag{48}$$

where s_i is the average spacing of the ith set of fractures. If we neglect the hydraulic conductivity of the rock matrix and the connectivity of the factures, and define

$$b_i = \frac{1}{m_i}\sum_{j=1}^{m_i} f(\beta_{ij}) b_{0ij} \quad \text{and} \quad s_i^{-1} = \frac{\pi}{V_p}\sum_{j=1}^{m_i} r_{ij}^2 \tag{49}$$

Then, the formulation presented in Eq. (47) is totally equivalent to Snow's formulation, Eq. (48).

On the other hand, the Oda's formulation is described by

$$\mathbf{K} = \varsigma(P_{kk}\boldsymbol{\delta} - \mathbf{P}) \tag{50}$$

where $\boldsymbol{P}$ is the fracture geometry tensor, with $P_{kk} = P_{11}+P_{22}+P_{33}$.

$$\mathbf{P} = \pi\rho\int_0^\infty\int_0^\infty\int_\Omega r^2 b^3 \mathbf{n}\otimes\mathbf{n} E(n,r,b)\mathrm{d}\Omega\mathrm{d}r\mathrm{d}b \tag{51}$$

where $E(n, r, b)$ is a probability density function of the geometry of the fractures, ρ is the number of fracture centers per unit of volume, with $\rho = m_v / V_p$, $m_v = \sum m_i$, and ς is the dimensionless scalar adopted to penalize the permeability of real fractures with roughness and asperities. Assuming that a statistically valid *REV* exists and being aware that the fracture orientation is a discrete event, the fracture geometry tensor may be empirically constructed by the following direct summation

$$\mathbf{P} = \frac{\pi}{V_{\mathrm{p}}} \sum_{i=1}^{m_{\mathrm{v}}} r_i^2 b_i^3 \mathbf{n}_i \otimes \mathbf{n}_i \tag{52}$$

Following a similar deduction, it can be inferred that all these three formulations are equivalent not only in form but also in function, though they are derived from different approaches and different assumptions. The formulation presented in Eq. (47) can be directly obtained from Snow's formulation by considering the connectivity and roughness of the fractures and integrating the aperture changes under engineering disturbance. The discretized form of the Oda's formulation is much closer to the current formulation, and the latter can also be directly achieved from the former by considering the connectivity of the fracture network. However, the proposed method for formulating an equivalent hydraulic conductivity tensor for complex rock mass based on the superposition principle of liquid dissipation energy is a widely applicable approach not only to equivalent continuum but also to discrete medium.

4.4 A numerical example: hydraulic conductivity of the rock mass in the Laxiwa Hydropower Project

In order to validate the theoretical model presented in Section 4.2, we investigated the hydraulic conductivity of a fractured rock mass at the construction site of the Laxiwa Hydropower Project, the second largest hydropower project on the upstream of the Yellow River. The selected construction site for a double curvature arch dam is a V-shaped valley formed by granite rocks, as shown in Fig. 14. The dam height is 250 m, the top elevation of the dam is 2460 m, the reservoir storage capacity is 1.06 billion m^3 and the total installed capacity is 4200 MW.

A typical section of the Laxiwa dam site is illustrated in Fig. 15. Besides faults, four sets of critically oriented fractures are developed in the rock mass at the construction site. The geological characteristics of the fractures are described by spacing, trace length, aperture, azimuth, dip angle, the joint roughness coefficient, *JRC*, of the fractures as well as the connectivity of the fracture network (i.e., the number of fractures intersected by one fracture). According to site investigation, the statistics (i.e., the averages and the mean squared deviations, as well as the distribution of the characteristics) of the fractured rock mass on the right bank of the valley are listed in Table 3.

Fig. 14. Site photograph of the Laxiwa valley

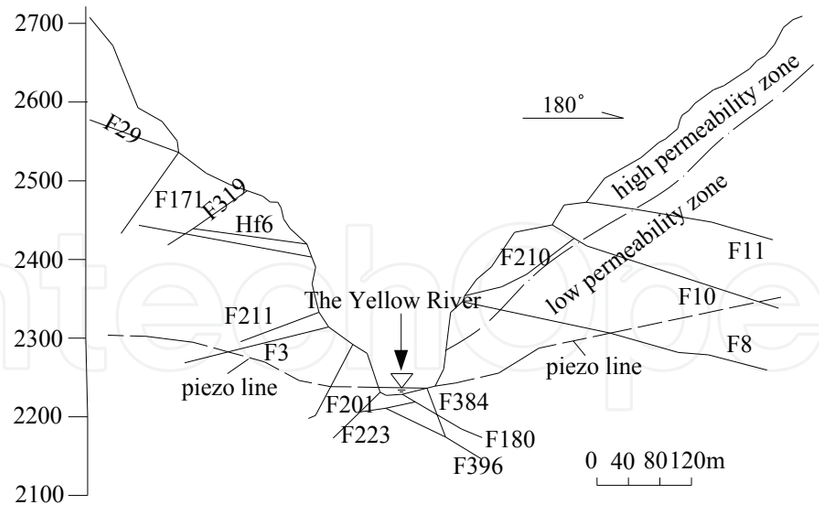

Fig. 15. A typical section of the Laxiwa dam site

Set	Spacing (m)	Length (m)		Aperture (mm)		Azimuth (°)		Dip (°)		Connectivity	
		avg.	dev.	avg.	dev.	avg.	dev.	avg.	dev.	avg.	dev.
1	1.45	5	1.5	0.096	0.02	85.3	10	54.5	10	5	3
2	2.62	3	1.0	0.096	0.02	355.1	20	29.8	5	3	2
3	10.96	3	1.0	0.096	0.02	287.4	20	61.4	10	3	2
4	10.96	3	1.0	0.096	0.02	320.2	20	11.9	5	3	2
Distribution	logarithmic normal	negative exponential		Gama		normal		normal		normal	

*'avg.' denotes arithmetic mean of a variable,
'dev.' represents root mean squared deviation

Table 3. Characteristic variables of the fractured rock mass*

At the construction site of the Laxiwa dam, a total number of 1450 single-hole packer tests were conducted to measure the hydraulic properties of the rock mass, with 113 packer tests for the shallow rock mass on the right bank in 0–80 m horizontal depth and 278 packer tests for the deeper rock mass. The measurements of the hydraulic conductivity range from 10^{-5} cm/s to 10^{-6} cm/s for the shallow rock mass and from 10^{-6} cm/s to 10^{-7} cm/s for the deeper rock mass, with in average 4.94×10^{-5} cm/s for the former and 3.80×10^{-6} cm/s for the latter, respectively (Liu, 1996). On the other hand, in-situ stress tests showed that the geostress in the base of the valley and in deep rock mass has a magnitude of 20–60 MPa, with the direction of the major principal stress pointing towards NNE. As a result of stress release, the release fractures are frequently developed and a high permeability zone of 0–80 m horizontal depth is formed in the bank slope, as shown in Fig. 15. The stress release fractures, however, become infrequent in deeper rock mass, and the measured hydraulic conductivity is generally 1–2 orders of magnitude smaller than the hydraulic conductivity of the rock mass in shallow depth away from the bank slope. Therefore, the hydraulic conductivity of the rock mass at the construction site of the Laxiwa arch dam is mainly controlled by the fracture network and the stress state.

Based on these statistics given in Table 3, fracture networks can be generated and calibrated for the rock mass at the construction site of the Laxiwa Hydropower Project using the Monte-Carlo method by assuming that each fracture is a smooth, planar disc, with its center uniformly distributed in the simulated area. For each set of fractures, the geometrical parameters of any one are sampled by Monte-Carlo method until enough fractures are included in the simulated area. Then, a calibration procedure is invoked to check whether the generated model satisfies the distribution mode of the real fracture network. If doesn't, the fracture network will be regenerated until one matches the distribution mode. With the generated fracture network, the actual connectivity can be computed by spatial operation on the fractures. But for calibrated fracture network, a more convenient approximate approach to determine the connectivity of the fracture network, as it is adopted here, is to directly produce ξ_{ij} in Eq. (42) with the Monte-Carlo method and the characteristics presented in Table 3, then W_{ij} is derived from Eq. (42) with $\overline{\xi}_i$, the maximum number of fractures cut by the ith set of fractures. Field measurements are used to estimate $\overline{\xi}_i$, with $\overline{\xi}_1$=11, $\overline{\xi}_2$=8 and $\overline{\xi}_3 = \overline{\xi}_4$=6 for the four sets of fractures, respectively. Fig. 16 illustrates a simulated fracture network with size of 20×20×20 m.

On the basis of the fracture network generated above, we compute the hydraulic conductivity tensor for the simulated cubic volume of rock mass with size of 20×20×20 m using the method given by Snow (1969) and the method presented in Section 4.2, respectively. To show the coupling effect of stress/deformation on hydraulic properties, we consider two scenarios for examination. In the first scenario, we consider the fracture network located in the shallow depth away from the bank slope, where the impact of the in-situ stress is negligible. While in the second scenario, the fracture network is situated in larger depth, and a typical stress state with $\sigma_x=\sigma_z$=10 MPa and σ_y=20 MPa is associated with it. Based on laboratory test results, the shear modulus of the fractures is estimated as μ=2 MPa, and then by taking the Poisson's ratio as ν=0.25, the Lame's constant is derived with λ=2 MPa. The kinematic viscosity of underground water is set to be $\nu_w=1.14\times10^{-6}$ m²/s and the frictional angle-like parameter and the normal stress-like parameter are taken as φ=0.4363 and $s=\sigma_n/20$.

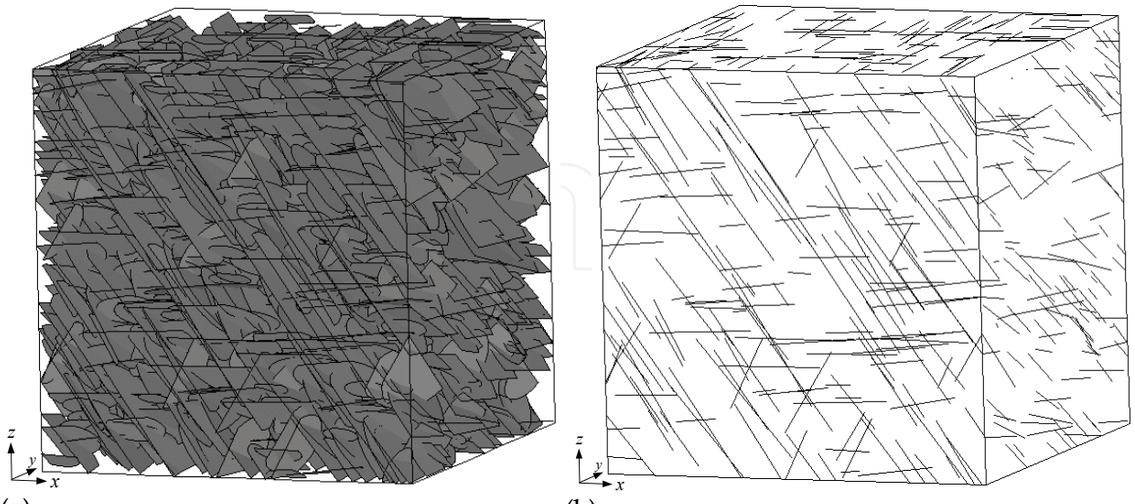

(a) (b)

Fig. 16. A three dimensional fracture network with size of 20×20×20 m generated by using the Monte-Carlo method for the rock mass in the Laxiwa Hydropower Project: (a) fracture network and (b) traces of the fractures on the surfaces of the simulated area

The predicted hydraulic conductivity tensor for the examined rock mass is listed in Table 4. From Table 4, one observes that for shallow rock mass (where the effect of in-situ stress is not considered), the Snow's method and the method presented in Section 4.2 predict similar results and the predicted hydraulic conductivity is in the magnitude of 10^{-5} cm/s and close to in-situ hydraulic observations, but the anisotropy in hydraulic conductivity manifests due to non-uniform distribution of fractures. Compared with the hydraulic conductivity of the shallow rock mass, the predicted hydraulic conductivity for the rock mass in larger depth with the same fracture network decreases in 2 orders of magnitude due to the closure of the fractures applied by the in-situ stresses, but the anisotropic property of the hydraulic conductivity remains, which suggests that the occurrence of the fractures has a significant impact on permeability. Taking into consideration the applied stress level, the reduction of hydraulic conductivity in orders of magnitude is very close to the results achieved in Min et al. (2004) through a discrete element method, and generally agrees with the in-situ hydraulic observations.

Snow's model (for shallow rock mass)		
4.78E–05	–4.76E–07	–1.71E–05
–4.76E–07	7.49E–05	–1.41E–05
–1.71E–05	–1.41E–05	4.08E–05
The proposed model (for shallow rock mass)		
1.93E–05	–1.75E–07	–6.39E–06
–1.75E–07	2.99E–05	–5.81E–06
–6.39E–06	–5.81E-06	1.64E–05
The proposed model (for deep rock mass)		
9.06E–08	–4.81E–09	–6.10E–08
–4.81E–09	1.85E–07	–1.92E–08
–6.10E–08	–1.92E–08	1.10E–07

Table 4. Predicted hydraulic conductivity tensor of the rock mass at the construction site of the Laxiwa dam (cm/s)

Now, we take for example the rock mass in shallow depth to estimate the *REV* size of the rock mass. For this purpose, the scale of the rock mass is increased gradually from 3×3×3 m to 40×40×40 m with an increment of 1 m in each dimension. In each step, a fracture network with prescribed size is generated by using the Monte-Carlo method described above, and it is worth noting that this method is somewhat different from the method used by Min & Jing (2003) and Long et al. (1982). For each fracture network, the hydraulic conductivity tensor is calculated from Eq. (47) and then the principal hydraulic conductivities are further obtained from the hydraulic conductivity tensor. The relationship between the computed principal hydraulic conductivities and the sizes of the rock mass is illustrated in Fig. 17. As we can see from Fig. 17, when the block size of the rock mass is smaller than 18×18×18 m, the population of fractures is not dense enough and the principal hydraulic conductivities fluctuate dramatically. On the other hand, as the size scales up to about 20×20×20 m, the examined rock mass has included enough fractures and the computed principal hydraulic conductivities approach a rather steady state, with k_1, k_2, k_3 estimated to be 2.41×10^{-5} cm/s, 3.59×10^{-5} cm/s, 1.08×10^{-5} cm/s, respectively. This suggests that the *REV* does exist in the rock mass and the rock mass can be regarded as an equivalent continuum medium as long as its size is no less than, e.g., 20×20×20 m or 8000 m^3.

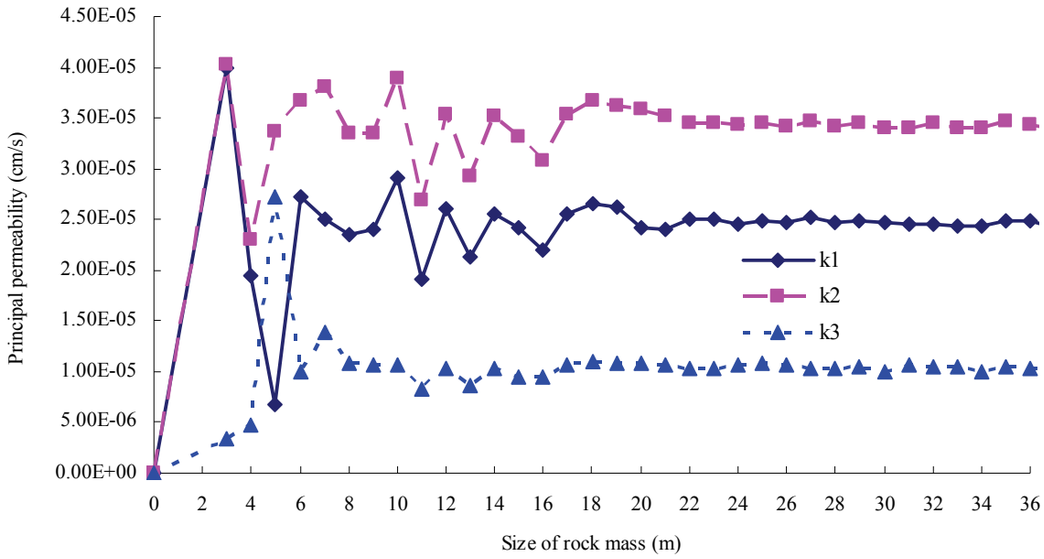

Fig. 17. Hydraulic conductivity versus the volume size of the fractured rock mass

5. Strain-dependent hydraulic conductivity tensor of fractured rocks

On the basis of the strain-dependent model presented in Section 3 for rock fractures, this section formulates the strain-dependent hydraulic conductivity tensor for fractured rock masses cut by one or multiple sets of parallel fractures. The major difference between the model in this section and the stress-dependent model presented in Section 4 is that the former is capable of describing influence of the post-peak mechanical behaviours on the hydraulic properties of the rock masses, and is suited for modelling the coupled processes in rock masses at high stress level and in drastic engineering disturbance condition.

5.1 An equivalent elasto-plastic constitutive model for fractured rocks

Consider a fractured rock mass cut by n sets of planar and parallel fractures of constant apertures with various orientations, scales and densities. The global response of the fractured rock mass under loading comes both from weak fractures and from stronger rock matrix. Based on this observation, an equivalent elasto-plastic constitutive model can be formulated by imposing assumptions on the interaction between fractures and rock matrix.

The coordinate systems are defined in the same way with those defined in Section 4.1 (see Fig. 13). Denote the unit vector along X_i-axis of the global frame as $\boldsymbol{e}_i$ (i=1, 2, 3) and the unit vector along x_i^f -axis of the fth local frame as $\mathbf{e}_i^f$ (i=1, 2, 3). Then, a second order tensor, $\boldsymbol{l}^f$, can be defined for transforming physical quantities between the frames, with the components in the form of

$$l_{ij}^f = \mathbf{e}_i^f \cdot \mathbf{e}_j \tag{53}$$

Regarding the fractured rock mass as a continuous medium at the macroscopic scale, it is rational to assume that the global strain increment of the fractured rock mass is composed of the strain increments of rock matrix and fractures (Pande & Xiong, 1982; Chen & Egger, 1999), i.e.

$$\mathrm{d}\boldsymbol{\varepsilon} = \mathrm{d}\boldsymbol{\varepsilon}^{\mathrm{R}} + \sum_{\mathrm{F}} \mathrm{d}\boldsymbol{\varepsilon}^{\mathrm{F}} \tag{54}$$

where $\mathrm{d}\boldsymbol{\varepsilon}$, $\mathrm{d}\boldsymbol{\varepsilon}^{\mathrm{R}}$ and $\mathrm{d}\boldsymbol{\varepsilon}^{\mathrm{F}}$ are the total incremental strain tensor, the incremental strain tensor of rock matrix and the incremental strain tensor of *f*th set of fractures measured in the global coordinate system, respectively. Note that a variable with a superscript in upper case (i.e. R or F) means that it is measured in the $X_1X_2X_3$ system, while a variable with a superscript in lower case (i.e. *f*) is measured in $x_1^f x_2^f x_3^f$ system, respectively. Unless otherwise specified, the superscripts F and *f* are not summing indices.

On the other hand, traction continuity has to be ensured across the fracture interfaces. In the global coordinate system, this condition can be strictly represented by (Pande & Xiong, 1982; Chen & Egger, 1999)

$$\mathrm{d}\boldsymbol{\sigma} = \mathrm{d}\boldsymbol{\sigma}'^{\mathrm{R}} = \mathrm{d}\boldsymbol{\sigma}'^{\mathrm{F}} \tag{55}$$

where $\mathrm{d}\boldsymbol{\sigma}'$, $\mathrm{d}\boldsymbol{\sigma}'^{\mathrm{R}}$ and $\mathrm{d}\boldsymbol{\sigma}'^{\mathrm{F}}$ are the effective incremental stress tensor of the fractured rock mass, the effective incremental stress tensor of rock matrix and the effective incremental stress tensor of *f*th set of fractures, respectively. The effective stress tensor $\boldsymbol{\sigma}'$ is defined as

$$\boldsymbol{\sigma}' = \boldsymbol{\sigma} + \alpha p \boldsymbol{\delta} \tag{56}$$

where $\boldsymbol{\sigma}$ is the total stress tensor (positive for tension), p is the pore water pressure (positive for compressive pressure), and α ($\alpha \leq 1$) is an effective stress parameter.

Combining the plastic potential flow theory and the consistency conditions of rock matrix and fractures, an equivalent elasto-plastic constitutive model can be derived from Eqs. (54) and (55):

$$\mathrm{d}\boldsymbol{\varepsilon} = \mathbf{S}^{\mathrm{ep}} : \mathrm{d}\boldsymbol{\sigma}' \tag{57}$$

with

$$\mathbf{S}^{\mathrm{ep}} = (\mathbf{C}^{\mathrm{R,ep}})^{-1} + \sum_{\mathrm{F}} (\mathbf{C}^{\mathrm{F,ep}})^{-1} \tag{58}$$

where $\boldsymbol{S}^{\mathrm{ep}}$ is the equivalent elasto-plastic compliance tensor of the fractured rock mass.

$\boldsymbol{C}^{\mathrm{R,ep}}$ in Eq. (58) is the elasto-plastic modulus tensor of rock matrix. Neglecting the degradation of rock strength in the volume close to fracture intersections, $\boldsymbol{C}^{\mathrm{R,ep}}$ can be written as

$$\mathbf{C}^{\mathrm{R,ep}} = \mathbf{C}^{\mathrm{R}} - \frac{\mathbf{C}^{\mathrm{R}} : \dfrac{\partial Q_{\mathrm{R}}}{\partial \boldsymbol{\sigma}'} \otimes \dfrac{\partial F_{\mathrm{R}}}{\partial \boldsymbol{\sigma}'} : \mathbf{C}^{\mathrm{R}}}{\dfrac{\partial F_{\mathrm{R}}}{\partial \boldsymbol{\sigma}'} : \mathbf{C}^{\mathrm{R}} : \dfrac{\partial Q_{\mathrm{R}}}{\partial \boldsymbol{\sigma}'} + H_{\mathrm{R}}} \tag{59}$$

where $\boldsymbol{C}^{\mathrm{R}}$ is the fourth-order elastic modulus tensor of rock matrix, which can be represented in terms of the Lame's constants λ and μ:

$$C_{ijkl}^{\mathrm{R}} = \lambda \delta_{ij}\delta_{kl} + \mu(\delta_{ik}\delta_{jl} + \delta_{il}\delta_{jk}) \tag{60}$$

F_R, Q_R and H_R in Eq. (59) are the yield function, the plastic potential function and the hardening modulus of rock matrix, respectively. A non-associative flow rule with elastic-perfectly plasticity (i.e. H_R=0) is adopted for better modeling dilatant behavior of rock matrix by virtue of, for example, the Druker-Prager criterion with its cone fully inscribed by the Mohr-Coulomb hexagon, defined by functions

$$F_R = aI_1' + \sqrt{J_2} - \kappa = 0 \tag{61}$$

$$Q_R = \beta I_1' + \sqrt{J_2} \tag{62}$$

with

$$\alpha = \sin\varphi_R \,/\, \sqrt{3(3+\sin^2\varphi_R)} \tag{63}$$

$$\kappa = 3c_R \cos\varphi_R \,/\, \sqrt{3(3+\sin^2\varphi_R)} \tag{64}$$

$$\beta = \sin\psi_R \,/\, \sqrt{3(3+\sin^2\psi_R)} \tag{65}$$

where c_R and φ_R are the cohesion and the friction angle of rock matrix, respectively. I_1' and J_2 are the first invariant of the effective stress and the second invariant of the deviatoric stress of rock matrix, respectively. ψ_R is the mobilized dilatancy angle of rock matrix.

It should be noted here that in the literature, Drucker-Prager criterion has been used by many authors to model the elasto-plastic behaviour of intact rock matrix, see Pande & Xiong (1982) and Chen & Egger (1999) for example. Although a modified Drucker-Prager yield function may be more suitable for this formulation in order to model plastic deformation properties of intact rock such as pressure dependency, strain hardening, transition from compressibility to dilatancy and stress path dependency (Chiarelli et al., 2003), the criterion given above may keep the formulation compact and does not lose generality. Other yield functions, such as the modified Drucker-Prager criterion (Chiarelli et al., 2003) or the modified Hoek-Brown criterion (Hoek et al., 1992), can also be integrated into the formulation without major mathematical difficulties.

With the researches conducted by Yuan & Harrison (2004) and Alejano & Alonso (2005), the decaying process of the rock dilatancy angle in line with plasticity can be described by the following negative exponential expression through the equivalent plastic strain of rock matrix, $\bar{\varepsilon}_R^p$ (Lai, 2002):

$$\psi_R = \psi_R^{peak} \exp(-r_R \bar{\varepsilon}_R^p) \tag{66}$$

where $r_R \geq 0$ is a parameter for modelling the decaying process of the dilatancy angle, and ψ_R^{peak} is the peak dilatancy angle of rock matrix and the following expression has been proposed by recovering the shape of the peak dilatancy angle of fractures given by Barton & Bandis (1982) and by assuming $\psi_R^{peak} = \varphi_R$ for null confinement pressures (Alejano & Alonso, 2005):

$$\psi_{\mathrm{R}}^{\mathrm{peak}} = \frac{\varphi_{\mathrm{R}}}{1+\log_{10}\sigma_{\mathrm{c}}}\log_{10}\frac{\sigma_{\mathrm{c}}}{-\sigma_3'+0.1} \tag{67}$$

where σ_{c} is the unconfined compressive strength for intact rock. By Eqs. (66) and (67), the dependencies of rock dilatancy on plasticity, confining stress and scale are produced.

The equivalent plastic strain $\bar{\varepsilon}^{\mathrm{p}}$ is computed by the following:

$$\bar{\varepsilon}^{\mathrm{p}} = \int \mathrm{d}\bar{\varepsilon}^{\mathrm{p}} = \int \sqrt{\frac{2}{3}\mathrm{d}\boldsymbol{\varepsilon}^{\mathrm{p}} : \mathrm{d}\boldsymbol{\varepsilon}^{\mathrm{p}}} \tag{68}$$

Similarly, $\boldsymbol{C}^{\mathrm{F,ep}}$ in Eq. (58) is the elasto-plastic modulus tensor of *f*th set of fractures measured in the $X_1X_2X_3$ system, which can be calculated from its corresponding elasto-plastic modulus tensor measured in the $x_1^f x_2^f x_3^f$ system, $\boldsymbol{C}^{f,\mathrm{ep}}$, with the assumption of small strain and by imposing the following tensor transformation:

$$C_{ijkl}^{\mathrm{F,ep}} = l_{mi}^f l_{nj}^f l_{ok}^f l_{pl}^f C_{mnop}^{f,\mathrm{ep}} \tag{69}$$

with

$$\mathbf{C}^{f,\mathrm{ep}} = \mathbf{C}^f - \frac{\mathbf{C}^f : \dfrac{\partial Q_f}{\partial \boldsymbol{\sigma}'} \otimes \dfrac{\partial F_f}{\partial \boldsymbol{\sigma}'} : \mathbf{C}^f}{\dfrac{\partial F_f}{\partial \boldsymbol{\sigma}'} : \mathbf{C}^f : \dfrac{\partial Q_f}{\partial \boldsymbol{\sigma}'} + H_f} \tag{70}$$

where $\boldsymbol{C}^f$ is the fourth-order tangential elastic modulus tensor of the *f*th set of fractures, with $C_{3333}^f = s_f k_{\mathrm{nf}}$, $C_{2323}^f = C_{3131}^f = s_f k_{\mathrm{sf}}$, and with all other elements equal to zero. The symbols k_{nf}, k_{sf} and s_f are the normal stiffness, the tangential stiffness and the spacing of the *f*th set of fractures, respectively. The expressions for the elements in $\boldsymbol{C}^f$ mean that the strain of fractures is evaluated over the fracture spacing, not over the fracture aperture, thus enabling the proposed model to consider the post-sliding plasticity of fractures and nonlinear variations of k_{nf} and k_{sf} with dilatancy caused by shear loading, without violating the small strain assumption.

F_f, Q_f and H_f in Eq. (70) are the yield function, the plastic potential function and the hardening modulus of the *f*th set of fractures, respectively. The elasto-plastic behaviour of the fractures is treated in a similar fashion as that for the rock matrix, with a non-associative Mohr-Coulomb criterion:

$$F_f = \sqrt{\tau_{zxf}^2 + \tau_{zyf}^2} + \sigma_{zf}' \tan\varphi_f - c_f = 0 \tag{71}$$

$$Q_f = \sqrt{\tau_{zxf}^2 + \tau_{zyf}^2} + \sigma_{zf}' \tan\psi_f \tag{72}$$

where σ_{zf}', τ_{zxf} and τ_{zyf} are the effective normal stress and the shear stresses on the fracture surfaces, respectively. c_f, φ_f and ψ_f are the cohesion, the friction angle and the mobilized dilatancy angle of the *f*th set of fractures, respectively. Similar to Eq. (66), ψ_f is also a shrinking function of the equivalent plastic strain of fractures $\bar{\varepsilon}_f^{\mathrm{p}}$, and depends on normal stress and scale as well, in the following form:

$$\psi_f = \psi_f^{\text{peak}} \exp(-r_f \bar{\varepsilon}_f^{\text{p}}) \tag{73}$$

where r_f is the decaying parameter and ψ_f^{peak} is the peak dilatancy angle of the fth set of fractures, respectively, with the latter calculated by Eq. (26).
Thus at any loading step, as long as the stress increment of the equivalent rock mass, $\mathrm{d}\sigma'$, is obtained, the local strain pertinent to fth set of fractures can be derived as follows:

$$\mathrm{d}\boldsymbol{\varepsilon}^{\text{F}} = (\mathbf{C}^{\text{F,ep}})^{-1} : \mathrm{d}\boldsymbol{\sigma}' \tag{74}$$

and

$$\mathrm{d}\varepsilon_{ij}^{f} = l_{im}^{f} l_{jn}^{f} \mathrm{d}\varepsilon_{mn}^{\text{F}} \tag{75}$$

The separation of the incremental strain of fractures from that of the rock mass through the proposed equivalent constitutive model plays a significant role in the present study. It enables the formulation of strain-dependent hydraulic conductivity that accounts for the mobilized dilatancy behaviour, which will be demonstrated in the following section.

5.2 Strain-dependent hydraulic conductivity tensor for fractured rocks

Consider a domain of flow that has been discretized into several sub-domains according to rock quality classification. Suppose that each sub-domain contains n sets of fractures, with average initial aperture b_{f0} and spacing s_f for the fth set of fractures. Starting from Eq. (22) and using the averaging concept for the hydraulic conductivity over the whole sub-domain, the equivalent initial hydraulic conductivity of the fth set of fractures, k_{f0}, in the examined sub-domain can be represented as (Castillo, 1972; Liu et al., 1999)

$$k_{f0} = \varsigma \frac{g b_{f0}^3}{\nu s_f} \tag{76}$$

where ς, as pointed out before, is a dimensionless constant introduced to penalize the real water conducting capacity of natural fractures with rough walls, finite scales, asperity areas and filling materials. The validity of using a constant value of ς has been examined by Zhou et al. (2006).
Assuming that the change in spacing s_f during modeling is negligible, under normal and shear stress loadings we have

$$k_f = \varsigma \frac{g b_f^3}{\nu s_f} = \varsigma \frac{g (b_{f0} + \Delta b_f)^3}{\nu s_f} \tag{77}$$

where Δb_f and k_f are the increment of the aperture and the equivalent hydraulic conductivity of the fth set of fractures under loading, respectively. Suppose that strain localization (Lai, 2002; Vajdova, 2003) is not dominantly exhibited in the concerned fractures, it is approximately valid that

$$\Delta b_f = s_f \Delta \varepsilon_{zf} \tag{78}$$

where $\Delta\varepsilon_{zf}$ is the increment of the normal strain of the fth set of fractures, which can be directly obtained from Eq. (75).
Substituting Eq. (78) into Eq. (77) then yields

$$k_f = k_{f0}\left(1+\frac{s_f}{b_{f0}}\Delta\varepsilon_{zf}\right)^3 \tag{79}$$

Following the theory proposed by Snow (1969), a strain-dependent equivalent hydraulic conductivity tensor for fractured rock masses with n sets of fractures is represented by

$$\mathbf{K} = \sum_f k_f(\boldsymbol{\delta}-\mathbf{n}_f\otimes\mathbf{n}_f) = \sum_f k_{f0}\left(1+\frac{s_f}{b_{f0}}\Delta\varepsilon_{zf}\right)^3(\boldsymbol{\delta}-\mathbf{n}_f\otimes\mathbf{n}_f) \tag{80}$$

where $\boldsymbol{K}$ is the equivalent hydraulic conductivity tensor of the examined rock mass, and $\boldsymbol{n}_f$ is the unit vector normal to the fth set of fractures.
The following significant implications can be observed from the formulation of $\boldsymbol{K}$ in Eq. (80):

1. $\boldsymbol{K}$ is a cubic function of $\Delta\varepsilon_{zf}$, and any variation in ε_{zf} under loading will trigger the change in $\boldsymbol{K}$, even in orders of magnitude. This exactly accounts for the coupling effect of mechanical loading (strain/stress) on hydraulic properties.
2. $\boldsymbol{K}$ depends on incremental strains, rather than on stresses, which makes it possible to integrate various material nonlinearities in hydro-mechanical coupling analysis.
3. In addition to cubic relation, the influence of $\Delta\varepsilon_{zf}$ on $\boldsymbol{K}$ is amplified by s_f/b_{f0}, indicating that $\boldsymbol{K}$ can be rather sensitive to b_{f0} and s_f. Therefore, techniques for estimating b_{f0} and s_f need to be carefully developed, on the basis of laboratory or in-situ hydraulic test data.
4. The orientations of fractures possibly render $\boldsymbol{K}$ highly anisotropic, even if $\boldsymbol{K}$ is initially assumed isotropic, as has been systematically examined, e.g. by Liu et al. (1999).
5. When implemented in a FEM code, a different $\boldsymbol{K}$ can be associated to each geological sub-domain or even to each element, as long as k_{f0}, b_{f0} and s_f for the sub-domains or elements can be estimated in advance.
6. As a nature of the homogenized equivalent continuum approach, the size effect of fractures, especially the size-dependency of aperture, is not fully considered in the formulation of $\boldsymbol{K}$ for simplicity, even though it can be reflected to some degree through ς and scaled *JRC* and *JCS* values. The connectivity and the intersection effect of fractures, on the other hand, may have a more significant influence on $\boldsymbol{K}$, but similarly, they cannot be properly considered in the equivalent continua without explicit representation of fractures. A rough remedy is to process the fracture system in such a way that only the connected fracture populations are included for conducting analyses.

To determine $\boldsymbol{K}$ of a fractured rock under any loading paths, a coupled hydro-mechanical process has to be invoked. With the assumption of incompressible rock matrix and fluid (e.g. groundwater), the governing equations for the coupled process of saturated fluid flow and deformation are given below as balance equation, geometric equation and fluid flow equation, respectively:

$$\sigma'_{ij,j} - \alpha p_{,i} + f_i = 0 \tag{81}$$

$$\varepsilon_{ij} = \frac{1}{2}\left(u_{i,j} + u_{j,i}\right) \tag{82}$$

$$\frac{\partial}{\partial x_i}\left(k_{ij}\frac{\partial h}{\partial x_j}\right) = \frac{\partial \varepsilon_{\mathrm{v}}}{\partial t} \tag{83}$$

where f_i and u_i are the components of the body force and displacement in the ith direction, $h=p/\gamma_{\mathrm{w}}+z$ the water head, z the vertical coordinate, γ_{w} the unit weight of water, and ε_{v} the volume strain of the rock mass.

In the coupled process given above, mechanical loading or disturbance to the rock mass results in change in flow properties and flow behaviour through Eqs. (80) and (83), while the change in flow behavior leads to change in mechanical response of the rock mass through Eq. (81). When the coupled process reaches a stable state, the solution to $\boldsymbol{K}$ is also available.

Now we briefly discuss how to determine k_{f0}, b_{f0} and s_f in Eq. (80) based on laboratory or in-situ hydraulic test or site investigation data. Obviously, the initial hydraulic conductivity, k_{f0}, can be determined by in-situ hydraulic tests. Suppose the initial hydraulic conductivity tensor, $\boldsymbol{K}_0$, is known through in-situ hydraulic test, as suggested by Hsieh & Neuman (1985), then $\boldsymbol{K}_0$ can be rewritten, from Eq. (80), in the following form:

$$\mathbf{K}_0 = \sum_f k_{f0}(\boldsymbol{\delta} - \mathbf{n}_f \otimes \mathbf{n}_f) \tag{84}$$

By optimizing Eq. (84), k_{f0} (f=1, …, n) can be estimated if the number of the sets of critically oriented fractures, n, is less than or equal to 6 (i.e. the number of the independent components of $\boldsymbol{K}_0$), regardless $\boldsymbol{K}_0$ is assumed to be isotropic or anisotropic.

The average spacing of the fth set of fractures, s_f, can be roughly estimated from the statistics of drill holes or scanlines. An alterative, however, is to use *RQD* (Rock Quality Designation) for determining s_f, as suggested by Liu et al. (1999), when the value of *RQD* for a specific rock mass is known *a priori*.

After the initial hydraulic conductivity, k_{f0}, and the average spacing, s_f, of the fractures are determined, the mean initial aperture of the fractures, b_{f0}, is ready to be back-calculated from Eq. (76).

5.3 Validation of the proposed model

5.3.1 Hydraulic conductivity of the surrounding rock of a circular tunnel in the Stripa mine

Here we compare the proposed method with results from a previous study as presented by Liu el al. (1999) by applying the method to an excavated circular tunnel with a biaxial stress field, σ_x and σ_z. The physical model is illustrated in Fig. 18, which is actually a manifestation of the reality of the Stripa mine in Sweden (Kelsall et al., 1984; Pusch, 1989). The following description about the tunnel is directly taken from Liu et al. (1999):

A Buffer Mass Test was conducted in Stripa Mine over the period 1981-1985 (Kelsall et al., 1984; Pusch, 1989) to measure the permeability of a large volume of low permeability fractured rock mass by monitoring water flow into a 33 m long section of the tunnel, as a large scale in-situ experiment for the research and development programs of underground geological disposal of nuclear wastes of the participating countries of the Stripa Project. The radius of the tunnel is about 2.5 m with two major sets of fractures striking obliquely to the

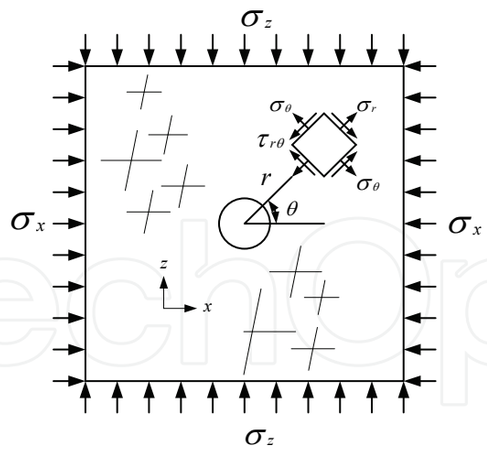

Fig. 18. Sketch of a circular excavation in a biaxial stressed rock mass.

tunnel axis, as shown in Fig. 18. Fracture frequency measured in holes drilled from the tunnel was on average 4.5 fractures/m in inclined holes and 2.9 fractures/m in vertical holes. The initial stress field is anisotropic with high horizontal stress component and the conductivity of the virgin rock is about 10^{-10} m/s. The excavation of the test drift produced a dramatic increase in axial hydraulic conductivity in a narrow zone adjacent to the periphery of the drift. The conductivity increase is estimated to be 3 orders of magnitude.

The following assumptions are made in the calculations, with some of them similar to those in Liu et al. (1999):

1. Statically uniform aperture and spacing distributions exist before excavation;
2. Fracture spacing and continuity are not altered by the excavation;
3. The high obliquity of the two major sets of fractures can be well approximated by two orthogonal sets of fractures;
4. Excavation-induced strain redistribution may be adequately captured by the proposed equivalent elasto-plastic constitutive model.

Some of the parameters are directly taken from Liu et al. (1999), while other unavailable parameters are assumed, as listed in Table 5, in which the initial mechanical aperture of the fractures is back-calculated from Eq. (76) by taking $k_0=10^{-10}$ m/s. Consistent with Liu et al. (1999), the far-field stress components are taken as σ_x=20 MPa and σ_z=10 MPa, respectively.

Category	Parameter	Setting
Intact rock matrix	Elastic modulus, E	37.5 GPa
	Poisson's ratio, ν	0.25
	Cohesion, c_R	5 MPa
	Friction angle, φ_R	46°
Fractures	Initial mechanical aperture, b_0	0.0075 mm
	Spacing, s	0.27 m
	Normal stiffness, k_n	200 GPa/m
	Shear stiffness, k_s	100 GPa/m
	Dimensionless constant, ς	0.0067
	Cohesion, c_f	0.4 MPa
	Friction angle, φ_f	40°

Table 5. Geometrical and mechanical parameters for a circular tunnel

To avoid the difficulty in determining the initial dilatancy angles and the corresponding decay parameters of fractures and intact rock matrix, associative flow rule is used in this simulation. Again for simplicity, both the normal stiffness and the shear stiffness of the fractures are assumed constant during excavation. The finite element mesh of the model is shown in Fig. 19, and the FEM program was run to simulate the excavation effect of the tunnel. Fig. 20 shows the deformation zone and plastic zone of the rock mass after the tunnel excavation. Fig. 21 plots the excavation-induced changes in hydraulic conductivities around the circular tunnel, which are directly compared with the results presented in Liu et al. (1999).

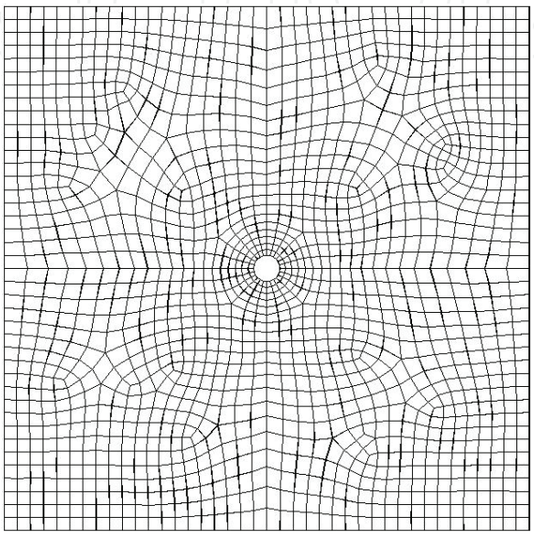

Fig. 19. Finite element mesh for simulation of a tunnel excavation.

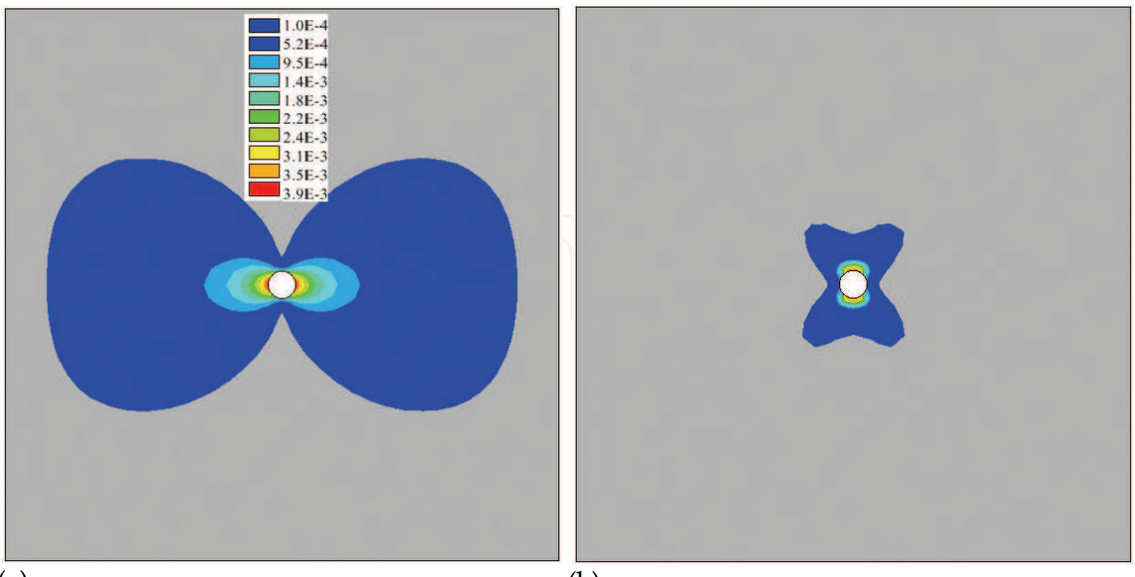

(a) (b)

Fig. 20. Deformation zone and plastic zone induced by the tunnel excavation: (a) deformation zone and (b) plastic zone

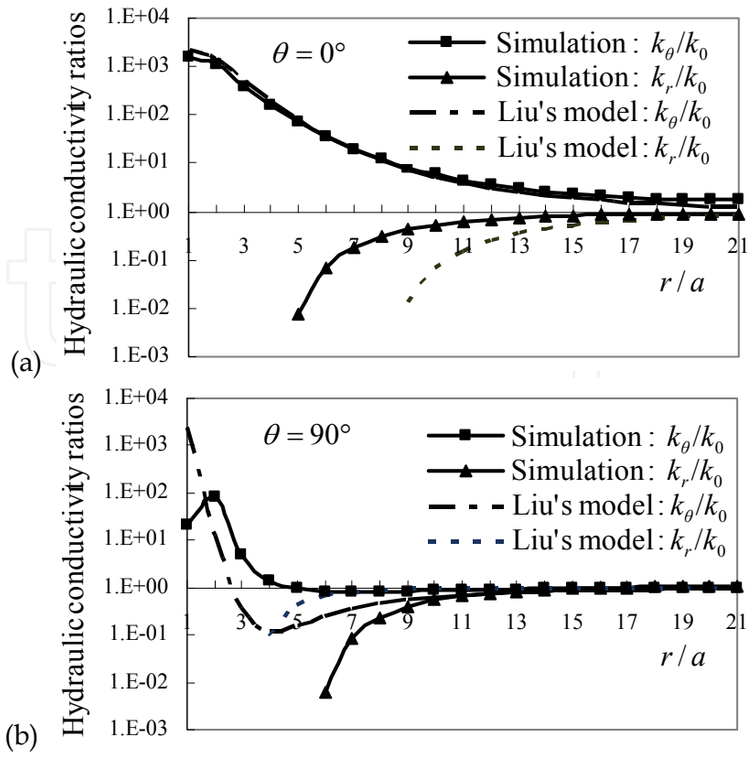

Fig. 21. Excavation-induced hydraulic conductivity ratios around a circular tunnel in a biaxial stressed rock mass, where a is the radius of the tunnel and r is the distance away from the tunnel center. θ=0° denotes the horizontal direction while θ=90° the vertical direction.

It can be observed from Fig. 21 that generally tangential conductivities are found to increase greatly due to the formation of the excavation disturbed zone around the tunnel, while radial conductivities diminish greatly as a result of closure on related fractures. In the horizontal direction (i.e. θ=0°), the excavation-induced tangential hydraulic conductivity ratios, k_θ/k_0, predicted by our model are very close to the results presented in Liu et al. (1999). For radial hydraulic conductivity ratios, k_r/k_0, however, deviation occurs in the vicinity of the excavation. Such a deviation is also found both for k_θ/k_0 and for k_r/k_0 in the vertical direction (i.e. θ=90°).

Clearly, these deviations are largely resulted from the facts that (1) Different strain distribution patterns are assumed in the elastic model in Liu et al. (1999) and in our elasto-plastic model; (2) Different methods are used to compute the strain increments of fractures. In Liu et al. (1999), normal strains of fractures were separated from rock matrix through a modulus reduction ratio empirically defined as a function of *RMR*, while in this simulation fracture strains were calculated by strain decomposition through an equivalent elasto-plastic constitutive model; (3) Radial and tangential fractures were assumed in Liu et al. (1999), leading to different background fracture networks; and (4) As mentioned above, some of the parameters, such as the shear strength of fractures and rock matrix, the shear stiffness and normal stiffness of the fractures, are unavailable in the literature (Kelsall et al., 1984; Pusch, 1989; Liu et al., 1999) and hence are empirically assumed in the calculations. If these

parameters are determined based on in-situ or laboratory experiments, more convincing results may be achieved.

Despite the deviations, the trends of variation of the hydraulic conductivity ratios around the tunnel due to excavation are consistent between the two studies, and basically accord with the in-situ experimental observations, demonstrating the applicability of the present model in this section.

From Fig. 20, one observes that the excavation-induce deformation zone and plastic zone are asymmetric, due to the anisotropic initial stress field. As a result, the predicted hydraulic conductivities are highly anisotropic due to strain redistribution, as shown in Fig. 21. In the horizontal direction (i.e. θ=0°), the deformation zone extends as far as more than 16 times of the tunnel radius and the plastic zone extends 2 times of the tunnel radius, while in the vertical direction (i.e. θ=90°), they are, respectively, within 2 and 5 times of the tunnel radius. The asymmetry of deformation zone and plastic zone demonstrates why the predicted hydraulic conductivities approach k_0 more slowly in the horizontal direction than in the vertical direction. The changes in hydraulic conductivities resulted from strain redistribution in the disturbed rock mass indicate that a different hydraulic conductivity tensor should be associated to each geological sub-domain or even each element of the rock mass, which is important for hydro-mechanical coupling analyses.

5.3.2 Hydraulic conductivity of a cubic block of rock mass with three orthogonal sets of identical fractures

In this section, a numerical simulation is conducted to evaluate hydraulic behaviour of a cubic block of rock mass containing three orthogonal sets of identical fractures under isotropic triaxial compression and shear loading. The primary goal is to investigate the change in the hydraulic conductivity of the rock mass with increasing shear load, which is obviously not achievable through any elastic models considering only the deformation of fractures under normal stresses, e.g. in Liu et al. (1999).

The underlying rock mass block model for examination, with a size of 10×10×10 m (a scale that can represent both the initial mechanical and hydraulic *REV*s (Min et al., 2004)), is assumed to contain three orthogonal sets of identical fractures, as sketched in Fig. 22. The spacing, s, of each set of fractures and the initial aperture, b_0, of each fracture are assumed to be identical, with s=1 m and b_0=1 mm. The mechanical properties of each fracture are also regarded identical and for simplicity, both the normal stiffness and the shear stiffness of the fractures are assumed to be constant during shear loading. All parameters used in this simulation are listed in Table 6, and such parameter settings enable us to demonstrate how the hydraulic conductivity evolves from initial isotropy to anisotropy in the shearing process.

The examined rock mass block model is divided into 1000 brick elements, and the resultant mesh is shown in Fig. 22. The loading condition is as follows. First, triaxial compressive stresses are applied on the surfaces of the cubic block, with $\sigma_x=\sigma_y=\sigma_z$=20 MPa. Then, a shearing load , τ, is applied on the upper and lower surfaces of the block model step by step, increasing at an increment of 1 MPa until a maximum shear load, 20 MPa, is reached. At each step of shear loading, numerical divergence may occur. If numerical divergence does occur, the simulation program terminates after 1000 iterations with a modified Newton-Raphson method.

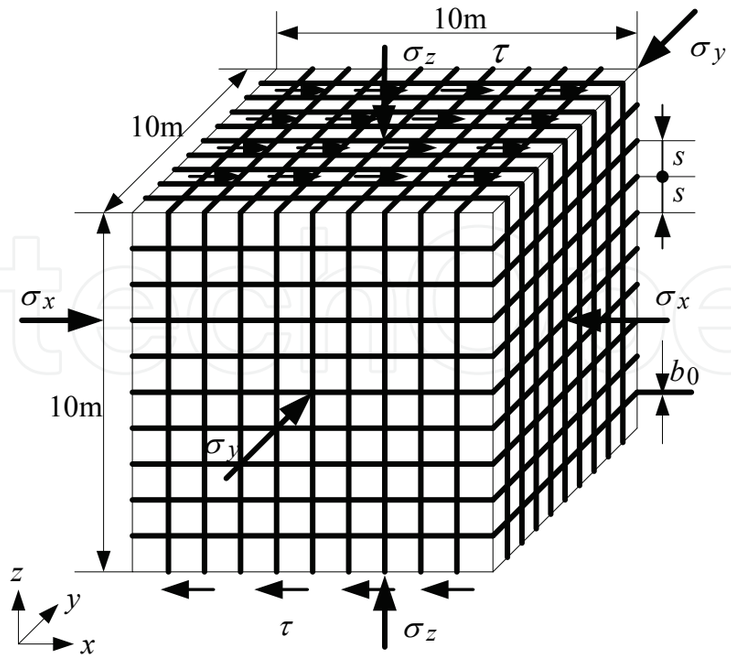

Fig. 22. Sketch of a cubic block of rock mass with three orthogonal sets of identical fractures

Category	Parameter	Setting
Intact rock matrix	Elastic modulus, E	6 GPa
	Poisson's ratio, ν	0.25
	Cohesion, c_R	1 MPa
	Friction angle, φ_R	46°
	Peak dilatancy angle, ψ_R^{peak}	35°
	Decay parameter of dilatancy, r_R	100
Fractures	Initial mechanical aperture, b_0	1 mm
	Spacing, s	1 m
	Normal stiffness, k_n	30 GPa/m
	Shear stiffness, k_s	10 GPa/m
	Dimensionless constant, ς	0.0067
	Cohesion, c_f	0.4 MPa
	Friction angle, φ_f	40°
	Peak dilatancy angle, ψ_f^{peak}	26°
	Decay parameter of dilatancy, r_f	100

Table 6. Geometrical and mechanical parameters for a cubic block of fractured rock mass

Clearly, before the rock mass is loaded, its initial hydraulic properties are isotropic, with $k_{x0}=k_{y0}=k_{z0}=1.30\times10^{-2}$ cm/s by Eq. (84). Under the condition of isotropic compression, the rock mass remains elastic, the isotropic property of hydraulic conductivity is maintained, and the magnitude of the hydraulic conductivity reduces by 2 orders of magnitude due to compression of fractures, with $k_x=k_y=k_z=4.82\times10^{-4}$ cm/s by Eq. (80). When shear stress is added incrementally on the rock mass block model from 0 to 20 MPa, the proposed method

predicts some interesting results, as depicted in Table 7, Figs. 23 and 24, respectively. Table 7 and Fig. 23 show the major hydraulic conductivities of the rock mass and Fig. 24 shows a typical case of mobilized dilatancy angle of a fracture under increasing shear loading.

As can be observed from Fig. 23, shear load has a substantial impact on the evolution of hydraulic conductivity of the rock mass model. Before the shear load reaches 4 MPa, the response of the rock mass model remains elastic, and the hydraulic conductivity components of the rock mass model are basically identical and do not vary with the shear load. When the shear load exceeds 4 MPa, however, hydraulic conductivity of the model becomes anisotropic. Due to shear dilation of fractures in the z-direction, the major hydraulic conductivities parallel to the direction of shear load in x-y plane, k_x and k_y, increase mildly at first when the shear load is smaller than 8 MPa. Afterwards, they increase dramatically, reaching an increase of 3-4 orders of magnitude. They approach a relatively stable state after the shear load increases up to 14 MPa. Obviously, the increase of k_x and k_y is resulted from the dilatancy behavior of the fractures related to equivalent plastic strain, as shown in Fig. 24, where the mobilized dilatancy angle approaches zero as the shear load approaches 14 MPa. When the shear load exceeds 14 MPa, shear dilatancy of the related fractures becomes trivial and hence k_x and k_y become steady. From Table 7 and Fig. 23, we can further see that k_x and k_y are very close to each other in values and they generally have the same varying trend with the increasing shear load.

τ (MPa)	k_x (cm/s)	k_y (cm/s)	k_z (cm/s)	τ (MPa)	k_x (cm/s)	k_y (cm/s)	k_z (cm/s)
-	0.013016	0.013016	0.013016	10	0.279373	0.279350	0.000020
0	0.000482	0.000482	0.000482	11	1.088835	1.088816	0.000056
1	0.000482	0.000482	0.000482	12	2.204162	2.204158	0.000375
2	0.000482	0.000482	0.000482	13	3.171558	3.171559	0.001374
3	0.000483	0.000483	0.000482	14	3.676801	3.697449	0.022811
4	0.000494	0.000486	0.000474	15	3.915193	4.137786	0.224877
5	0.000543	0.000509	0.000444	16	4.063688	4.696511	0.635383
6	0.000657	0.000576	0.000372	17	4.243447	5.407600	1.167070
7	0.000742	0.000643	0.000282	18	4.635512	6.233203	1.600997
8	0.000704	0.000581	0.000207	19	5.390907	7.316177	1.928768
9	0.012562	0.012459	0.000106	20	6.462514	8.618240	2.159053

Table 7. Major hydraulic conductivities of a cubic block of rock mass under isotropic compression and increasing shear loading

With the increase of shear load from 4 to 20 MPa, the change in the major hydraulic conductivity vertical to the direction of shear load, k_z, is even more interesting. Before the shear load reaches 10 MPa, k_z decreases significantly with increasing shear load and manifests a shear contraction-like behavior. When the shear load further increases, shear dilatancy occurs and k_z increases drastically, with changes in as high as 4-5 orders of magnitude. k_z reaches a relatively stable state after the shear load increases up to 17 MPa, which is actually a critical loading point that numerical instability may occur.

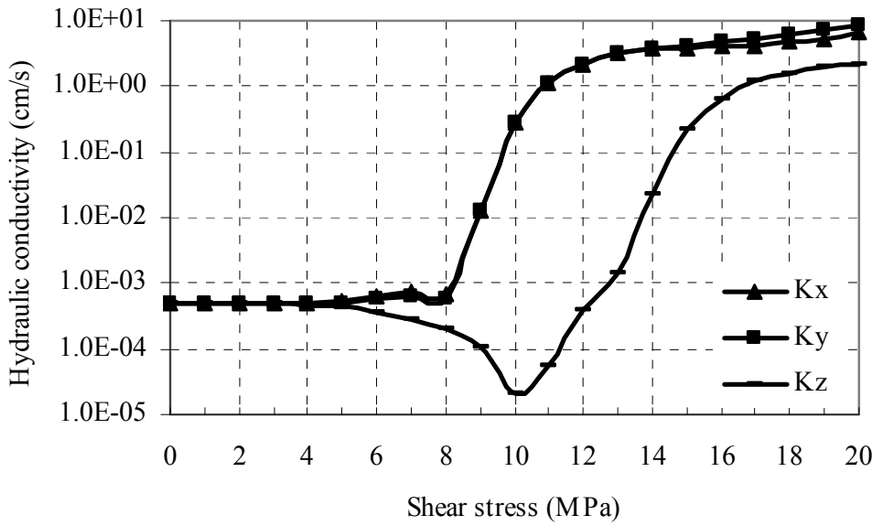

Fig. 23. Major hydraulic conductivities of a cubic block of rock mass with increasing shear load.

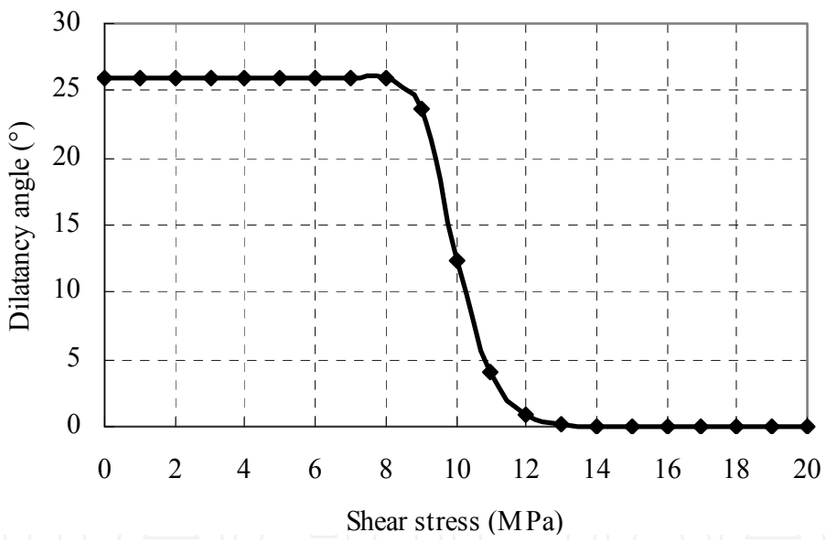

Fig. 24. A typical case of mobilized dilatancy angle of a fracture with increasing shear load.

6. Conclusions

In this chapter, mathematical models were developed to estimate the hydraulic conductivity tensor for fractured rock masses subjected to mechanical loading or engineering disturbance. Emphases are placed on the investigation of the geological characteristics of rock masses as well as the coupling between fluid flow and stress/deformation, especially the effect of shear dilation or shear contraction on the hydraulic behavior of rock fractures.

The stress-dependent hydraulic conductivity tensor was formulated by using the superposition principle of flow dissipation energy on the basis of the concept of representative elementary volume (*REV*) and the assumption that rock masses can be

treated as equivalent continuum media. The deformation behaviours of rock fractures subjected to normal and shear loadings are described with an elastic constitutive model, in which the pre-peak shear dilation or contraction of the fractures is empirically modelled. The validity of using the superposition principle of flow dissipation energy for development of the model is supported by the functional equivalence between the current formulation and the Snow's and Oda's models. This model is best suited for estimation of the hydraulic properties of rock masses at low stress level and with overall elastic response, and can be used to determine the applicability of the continuum approach to coupling analysis. The latter is achieved by performing numerical experiments to test the existence of the REV, and if exists, to further estimate the REV by gradually increasing the cubic volume of flow region, V_p, to see whether the hydraulic conductivity of the rock mass can eventually approach a steady point. The hydraulic properties and the REV size of the fractured rock mass at the construction site of the Laxiwa Hydropower Project were evaluated with the proposed model, and the calculation results were compared with the predictions of the Snow's model and validated by in-situ hydraulic tests, hence the feasibility of the proposed model in rock engineering practices is demonstrated.

The strain-dependent hydraulic conductivity tensor, on the other hand, was developed for disturbed rock masses under excavation or loading. In the model, a non-associative elastic-perfectly plastic constitutive model was integrated to describe the deformation behaviours of the rock masses by characterizing them as equivalent continua containing one or multiple sets of parallel fractures. The clear advantages of the formulation are:

- The proposed hydraulic conductivity tensor is related to strains rather than stresses, hence enabling easier hydro-mechanical coupling analysis to include the effect of material nonlinearity of fractured rock masses.
- Beneficial from the equivalent non-associative elastic-perfectly plastic constitutive model, the hydraulic conductivity tensor considers the impact of shear dilatancy of fractures on fluid flow properties via mobilized dilatancy angles.
- When reduced to one dimensional case with a single fracture under normal and shear loadings, a closed-form solution to the hydraulic conductivity can be obtained, enabling validation of the model by laboratory coupled shear-flow tests of rock fractures.
- The proposed model is easy to be implemented in a FEM code, particularly suitable for numerical analysis of coupled hydro-mechanical processes in rock engineering.

The closed-form solution was validated by an existing coupled shear-flow test, and the evaluation results show that the proposed solution can closely describe the hydraulic behavior of a hard rock fracture under a wide range of normal and shear loads. The results of the simulation conducted to predict the excavation-induced hydraulic conductivities around a circular tunnel in a biaxial stress field at the Stripa mine are justified by in-situ experimental observations and compared with an existing elastic strain-dependent model, which show that engineering disturbance such as underground excavations may dramatically alter the hydraulic conductivities of the rock mass surrounding the excavations and change the isotropic pattern of the initial hydraulic conductivities. The numerical simulation on a cubic block model of a rock mass with three orthogonal sets of identical fractures under isotropic triaxial compression and shear loading further demonstrates that shear loading may drastically change the hydraulic properties of fractured rocks, in the magnitude of as high as 4-5 orders, and lead to high anisotropy of the hydraulic properties.

Despite all these efforts, characterizing the hydraulic properties for fractured rock masses remains one of the most difficult research topics in rock mechanics. In the proposed models presented in this chapter, rock masses are assumed with rather regular distribution patterns of fractures, and the existence of a hydraulic conductivity tensor of the rock masses with any distribution of fractures is not discussed. The interaction between the fractures in the rock masses is also out of the scope of this chapter, and its effect on the hydraulic properties remains an open issue. Furthermore, the proposed models are established with a rather intuitive upscaling approach, and more rigorous homogenization schemes should be developed. All of there issues should be addressed in the future research.

7. Acknowledgements

The financial support from the National Natural Science Foundation of China (No. 51079107) and the National Natural Science Fund for Distinguished Young Scholars of China (No. 50725931), and the Program for New Century Excellent Talents in University (No. NCET-09-0610) for this study is gratefully acknowledged.

8. References

Alejano, L. R. & Alonso, E. (2005). Consideration of the dilatancy angle in rocks and rock masses. *International Journal of Rock Mechanics and Mining Sciences*, Vol. 42, No. 4, 481–507

Barton, N. (1976). Rock mechanics review: the shear strength of rock and rock joints. *International Journal of Rock Mechanics and Mining Sciences & Geomechanical abstracts*, Vol. 13, No. 9, 255-279

Barton, N. R. & Bandis, S. C. (1982). Effects of block size on the shear behaviour of jointed rocks. In: *Proc 23rd US Symp Rock Mechanics*, Berkeley

Barton, N.; Bandis, S. & Bakhtar, K. (1985). Strength, deformation and conductivity coupling of rock joints. *International Journal of Rock Mechanics and Mining Sciences & Geomechanical abstracts*, Vol. 22, No. 2, 121-140

Bear, J. (1972). *Dynamics of fluids in porous media*. American Elsevier, New York

Castillo, E. (1972). Mathematical model for two-dimensional percolation through fissured rock. In: *Proc Int Symp Percolation through Fissured Rock*, T1±D1–7, Stuttgart, Germany

Chen, Y. F.; Sheng, Y. Q. & Zhou, C. B. (2006). Strain-dependent permeability tensor for coupled M-H analysis of underground opening. *Proceedings of the 4th Asian Rock Mechanics Symposium*, pp. 271, Singapore, Nov 2006, World Scientific Publishing

Chen, Y. F.; Zhou, C. B. & Sheng, Y. Q. (2007). Formulation of strain-dependent hydraulic conductivity for fractured rock mass. *International Journal of Rock Mechanics and Mining Sciences*, Vol. 44, No. 7, 981-996

Chen, S. H. & Egger, P. (1999). Three dimensional elasto-viscoplastic finite element analysis of reinforced rock masses and its application. *International Journal for Numerical and Analytical Methods in Geomechanics*, Vol. 23, No. 1, 61–78

Chiarelli, A. S.; Shao, J. F. & Hoteit, N. (2003). Modeling of elastoplastic damage behavior of a claystone. *Int J Plasticity*, Vol. 19, 23–45

Esaki, T.; Du, S.; Mitani, Y.; Ikusada, K. & Jing, L. (1999). Development of a shear-flow test apparatus and determination of coupled properties for a single rock joint. *International Journal of Rock Mechanics and Mining Sciences*, Vol. 36, 641–50

Hoek, E.; Wood, D. & Shah, S. (1992). A modified Hoek-Brown criterion for jointed rock masses. In: *Proc Rock Characterization Symp ISRM: Eurock 92*, Hudson, J. A. (Ed.), 209–214, British Geotechnical Society, London

Hsieh, P. A. & Neuman, S. P. (1985). Field determination of the three-dimensional hydraulic conductivity tensor of anisotropic media. Water Resource Research, Vol. 21, No. 11, 1655–1665.

Huang, T. H.; Chang, C. S. & Chao, C. Y. (2002). Experimental and mathematical modeling for fracture of rock joint with regular asperities. Eng Fract Mech, Vol. 69, 1977–1996

Indelman, P. & Dagan, G. (1993). Upscaling of permeability of anisotropic heterogeneous formations. *Water Resources Research*, Vol. 29, No. 4, 917-923

Jing, L. (2003). A review of techniques, advances and outstanding issues in numerical modeling for rock mechanics and rock engineering. *International Journal of Rock Mechanics and Mining Sciences*, Vol. 40, No., 283-353

Jing, L.; Stephansson, O. & Nordlund, E. (1993). Study of rock joints under cyclic loading conditions. Rock Mechanics and Rock Engineering, Vol. 26, No. 3, 215–32

Kelsall, P. C.; Case, J. B. & Chabannes, C. R. (1984). Evaluation of excavation-induced changes in rock permeability. Int J Rock Mech Min Sci & Geomech Abstr, Vol. 21, No. 3, 123–35

Lai, T. Y. (2002). *Multi-scale finite element modeling of strain localization in geomaterials with strong discontinuity*. Ph.D. thesis, Stanford University

Liu, C. H.; Chen, C. X. & Fu, S. L. (2002). Testing study on seepage characteristics of single fracture with sand under shearing displacement. Chinese Journal of Rock Mechanics and Engineering, Vol. 21, No. 10, 1457-1461

Liu, J.; Elsworth, D. & Brady, B. H. (1999). Linking stress-dependent effective porosity and hydraulic conductivity fields to RMR. *International Journal of Rock Mechanics and Mining Sciences*, Vol. 36, 581-596

Liu, S. H. (1996). Generation of flow network and field tests on hydraulic conductivity for fractured rock mass. *Northwestern Hydropower*, Vol. 55, No. 1, 21-27

Lomize, G. M. (1951). *Flow in fractured rocks*. Gosenergoizdat, Moscow

Long, J. C. S.; Remer, J. S.; Wilson, C. R. & Witherspoon, P. A. (1982). Porous media equivalents for networks of discontinuous fractures. *Water Resource Research*, Vol. 18, No. 3, 645–58

Louis, C. (1971). A study of groundwater flow in jointed rock and its influence on the stability of rock masses. *Rock Mechanics Research Report*, No. 10, Imperial College of Science and Technology, London, Maini, YNT

Min, K. B. & Jing, L. (2003). Numerical determination of the equivalent elastic compliance tensor for fractured rock masses using the distinct element method. *International Journal of Rock Mechanics and Mining Sciences*, Vol. 40, No. 6, 795-816

Min, K. B.; Rutqvist, J.; Tsang, C. F. & Jing, L. (2004). Stress-dependent permeability of fractured rock masses: a numerical study. *International Journal of Rock Mechanics and Mining Sciences*, Vol. 41, No. 7, 1191-1210

Oda, M. (1985). Permeability tensor for discontinuous rock masses. *Geotechnique*, Vol. 35, No. 4, 483-195

Oda, M. (1986). An equivalent continuum model for coupled stress and fluid flow analysis in jointed rock masses. *Water Resources Research*, Vol. 22, No. 13, 1845-1856

Olsson, R. & Barton, N. (2001). An improved model for hydromechanical coupling during shearing of rock joints. *International Journal of Rock Mechanics and Mining Sciences*, Vol. 38, No. 3, 317-329

Pande, G. N. & Xiong, W. (1982). An improved multilaminate model of jointed rock masses. In: *Numerical Models in Geomechanics*, Dungar, R.; Pande, G. N. & Studer, J. A. (Ed.), 218–226, Bulkema, Rotterdam

Patir, N. & Cheng, H. S. (1978). An average flow model for determining effects of three-dimensional roughness on hydrodynamic lubrication. *ASME Journal of Lubrication Technology*, Vol. 100, 12-17

Plesha, M. E. (1987). Constitutive models for rock discontinuities with dilatancy and surface degradation. International Journal for Numerical and Analytical Methods in Geomechanics, Vol. 11, 345–62

Pusch, R. (1989). Alteration of the hydraulic conductivity of rock by tunnel excavation. *Int J Rock Mech Min Sci & Geomech Abstr*, Vol. 26, No. 1, 79–83

Snow, D. T. (1969). Anisotropic permeability of fractured media. *Water Resources Research*, Vol. 5, No. 6, 1273-1289

Vajdova, V. (2003). *Failure mode, strain localization and permeability evolution in porous sedimentary rocks*. Ph.D. thesis, Stony Brook University

Wang, M. & Kulatilake, P. H. S. W. (2002). Estimation of REV size and three dimensional hydraulic conductivity tensor for a fractured rock mass through a single well packer test and discrete fracture fluid flow modeling. *International Journal of Rock Mechanics and Mining Sciences*, Vol. 39, 887-904

Yuan, S. C. & Harrison, J. P. (2004). An empirical dilatancy index for the dilatant deformation of rock. *International Journal of Rock Mechanics and Mining Sciences*, Vol. 41, 679–86

Zimmerman, R. W.; Kumar, S. & Bodvarsson, G. S. (1991). Lubrication theory analysis of the permeability of rough-walled fractures. *International Journal of Rock Mechanics and Mining Sciences*, Vol. 28, No. 4, 325-331

Zhou, C. B.; Chen, Y. F. & Sheng, Y. Q. (2006). A generalized cubic law for rock joints considering post-peak mechanical effects. In: Proc GeoProc2006, 188–197, Nanjing, China

Zhou, C. B.; Sharma, R. S.; Chen Y. F. & Rong, G. (2008). Flow-Stress Coupled Permeability Tensor for Fractured Rock Masses. *International Journal for Numerical and Analytical Methods in Geomechanics*, Vol. 32, 1289-1309

Zhou, C. B. & Xiong, W. L. (1996). Permeability tensor for jointed rock masses in coupled seepage and stress fields. *Chinese Journal of Rock Mechanics and Engineering*, Vol. 15, No. 4, 338-344

Zhou, C. B. & Xiong, W. L. (1997). Influence of geostatic stresses on permeability of jointed rock masses. *Acta Seismologica Sinica*, Vol. 10, No. 2, 193-204

Zhou, C. B.; Ye, Z. T. & Han, B. (1997). A study on configuration and hydraulic conductivity of rock joints. *Advances in Water Science*, Vol. 8, No. 3, 233-239

Zhou, C. B. & Yu, S. D. (1999). Representative elementary volume (REV): a fundamental problem for selecting the mechanical parameters of jointed rock mass. *Chinese* Journal of Engineering Geology, Vol. 7, No. 4, 332-336

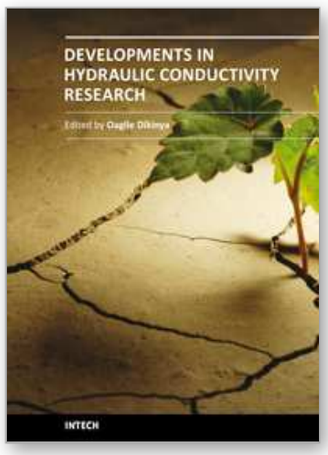

Developments in Hydraulic Conductivity Research

Edited by Dr. Oagile Dikinya

ISBN 978-953-307-470-2
Hard cover, 270 pages
Publisher InTech
Published online 28, February, 2011
Published in print edition February, 2011

This book provides the state of the art of the investigation and the in-depth analysis of hydraulic conductivity from the theoretical to semi-empirical models perspective as well as policy development associated with management of land resources emanating from drainage-problem soils. A group of international experts contributed to the development of this book. It is envisaged that this thought provoking book will excite and appeal to academics, engineers, researchers and University students who seek to explore the breadth and in-depth knowledge about hydraulic conductivity. Investigation into hydraulic conductivity is important to the understanding of the movement of solutes and water in the terrestrial environment. Transport of these fluids has various implications on the ecology and quality of environment and subsequently sustenance of livelihoods of the increasing world population. In particular, water flow in the vadose zone is of fundamental importance to geoscientists, soil scientists, hydrogeologists and hydrologists and allied professionals.

InTech Europe
University Campus STeP Ri
Slavka Krautzeka 83/A
51000 Rijeka, Croatia
Phone: +385 (51) 770 447
Fax: +385 (51) 686 166
www.intechopen.com

InTech China
Unit 405, Office Block, Hotel Equatorial Shanghai
No.65, Yan An Road (West), Shanghai, 200040, China
中国上海市延安西路65号上海国际贵都大饭店办公楼405单元
Phone: +86-21-62489820
Fax: +86-21-62489821

IntechOpen